UNIVERSITY OF TWENTE.

**Faculty of Electrical Engineering,
Mathematics & Computer Science**

Design improvement and prototyping of a Testbed for the Calibration and RFI Mitigation Algorithms used in OLFAR

J.J. Van 't Hof

B.Sc. Thesis
February 2016

Supervisors:
Dr. Ir. M.J. Bentum
Ir. P.K.A. van Vugt

Telecommunication Engineering Group
Faculty of Electrical Engineering,
Mathematics and Computer Science
University of Twente
P.O. Box 217
7500 AE Enschede
The Netherlands

Summary

A new generation of radio telescopes is being developed using nano satellite technology. A swarm of satellites can function together as one large radio telescope performing interferometry at frequencies below 30 MHz. These frequencies hold interesting insights in cosmology. Signals at these low-frequencies cannot be observed on Earth as they are blocked by Earth's ionosphere. In addition, the influences of man-made interference are less in space based telescopes.

The OLFAR (Orbiting Low Frequency Array) project is aimed at building such a radio telescope for exploring these low-frequencies. For OLFAR, new software algorithms are developed for the calibration and interference mitigation. To test these algorithms a testbed is to be developed which represents a swarm of satellites in OLFAR. The testbed is split up into five components: the observational antennas, an astronomical source simulator, the receivers, the software and the physical construction.

M. F. Brethouwer already performed a lot of work in designing and implementing the testbed during his master's thesis called *"Design of a Testbed for the Calibration and RFI Mitigation Algorithms used in OLFAR"*. The goal of this bachelor's assignment was to pick up where Brethouwer has left off and further implement the testbed.

During this thesis project a prototype of the Observational antenna system was constructed and characterized inside an anechoic chamber. The characterization concluded that the Observational antenna system meets al its specifications and can be used in the testbed.

A suitable signal generation method for the Astronomical source simulator has been found that uses a software defined radio (SDR). The benefit of using this SDR as the signal generator is that it is relatively cheap and also portable, allowing the testbed to be used in the field.

Research has been conducted into how the phase locked loop in the receivers of the testbed could be improved. A set of proposals is presented which would improve the synchronisation of the receivers to allow accurate measurements to be taken.

Some research was performed into improving the software. During this research improvements were found for synchronisation of the start of the measurement across the receivers of the testbed.

Finally a few concepts were created for the design of the physical construction of the testbed. These concepts were compared with the design of Brethouwer. It was concluded that one of the concepts combined with the ideas of Brethouwer would result into the most suitable design for the physical construction of the testbed.

With the work performed during this thesis project the development of the testbed is brought into a state where only the designs have to be finalized and implemented to complete it. No further research needs to be carried out, reducing the work left on the testbed to mainly the task of constructing the components and characterizing the testbed once completed.

Contents

List of acronyms

OLFAR	Orbitting Low Frequency Array
DCIS	Data Collection Colonies in Space
VLBI	Very Long Baseline Interferometry
PCB	printed circuit board
SMD	surface mount device
COTS	commercially off-the-shelf
LNA	low noise amplifier
VGA	variable gain amplifier
SNR	signal-to-noise ratio
VNA	vector network analyser
VSWR	voltage standing wave ratio
RFI	radio frequency interference
IFT	inverse Fourier transform
SDR	software defined radio
FPGA	field programmable gate array
PLL	phase locked loop
MIMO	multiple input multiple output
DAC	digital to analog converter
ADC	analog to digital converter
PD	phase detector
EMC	electro magnetic compatibilty

ADPLL all digitial phase locked loop

VCO voltage controlled oscillator

VCTCXO voltage controlled temperature compensated crystal oscillator

DCO digital controlled oscillator

FIR Finite Inpulse Response

IIR Infinite Impulse Response

TDC Time to Digital Converter

Chapter 1

Introduction

A new generation of radio telescopes is being developed. Using nano satellite technology it will soon be possible to deploy a swarm of satellites that can function together as one large radio telescope. One of the projects aimed at building such a radio telescope in space is Orbitting Low Frequency Array (OLFAR). For OLFAR new calibration and interference mitigation algorithms have to be developed. A testbed is to be constructed for testing and verifying these algorithms. The student M. F. Brethouwer already designed and implemented some parts of the testbed during his master's thesis project. In this thesis, the reader is provided with the documentation of the follow-up work that was performed during a bachelor's assignment in Electrical Engineering at the Telecommunication Engineering group of the University of Twente.

1.1 Context

Space telescopes have great advantages over Earth-based telescopes as they do not have to deal with the ionosphere of the Earth and the influences of man-made radio frequency interference (RFI) are less severe. This allows the space radio telescope to observe frequencies below 30 MHz that are of particular interest as they have never been properly observed before. For cosmology, observing this new frequency window will give scientists insight into the so-called Dark-Ages of the universe, between 0.4 million years and about 400 million years after the Big Bang. This is the time span in which the universe was opaque for visible light between the moment of cosmic microwave background radiation and the Epoch of Reionization [1].

Other applications of these low frequency radio telescopes are complementing measurements on (extra) galactic surveys, transients of solar or planetary bursts, X-ray binaries, pulsar signals and signals from (exo-)planets with a new frequency band [1].

The OLFAR project is aimed at building a radio telescope for exploring these low frequencies using a satellite swarm. To achieve sufficient spatial resolution the satellites of OLFAR fly in a swarm of 100 km in diameter [2]. To mitigate RFI, the satellites will be deployed on a location with low levels of interference. One such suited location would be a Moon orbit. At the backside of the Moon the satellites would be shielded from interference from the Earth and the Sun, which would make it a perfect location to conduct a sensitive measurement. Other options include orbits around some of the Earth-Moon or Sun-Earth Lagrange points, the sun or even a very high Earth orbit [1], [2].

Each of the satellites in OLFAR will contain low-frequency antennas and receivers to measure astronomical signals. This is done in a process called interferometry. To reduce the data that needs to be sent to Earth, the satellites perform a distributed correlation of the measurement signals [3]. To produce images using interferometry, OLFAR needs to be calibrated to take factors like antenna patterns, varying receiver gains and geometric delays into account. And since computational power is limited by the size of the satellites and limited available power, this calibration can only be done on Earth in post-processing. Additionally with OLFAR there are unique calibration challenges because the antennas are located in 3-dimensional swarm without any structure, instead of on plane as is the case in Earth based radio telescopes.

To perform these calibrations new algorithms are developed in the Data Collection Colonies in Space (DCIS) project. Currently P.K.A. Van Vugt is developing the algorithms for calibration of OLFAR during his PHd. research. At the moment, the algorithms are only tested in simulation, as there is no hardware of OLFAR yet. Therefore a testbed is to be constructed to test these algorithms on actual measured data. The testbed should give a realistic representation of OLFAR to include (unforeseen) non-ideal parameters that would not show up in simulations.

1.2 Framework

M. F. Brethouwer has already done a lot of work in designing and implementing the testbed during his master's assignment. He based the design choices for the testbed directly on the specifications of OLFAR. His work is documented in the thesis *"Design of a Testbed for the Calibration and RFI Mitigation Algorithms used in OLFAR"* [4]. The goal of this bachelors assignment was to pick up where Brethouwer left off and further implement the testbed.

1.3 Testbed outline

As was already mentioned the purpose of the testbed is to represent OLFAR to test calibration and RFI mitigation algorithms. However the testbed does not have to be an exact representation as some parts can be simplified. Brethouwer designed a testbed containing miniature satellite mock-ups, each with three orthogonal antennas as are also present on the satellites in OLFAR. The signals from the antennas are digitized by a set of receivers that send the measurement data to a computer. To mimic the movement of the satellites in OLFAR, the satellite mock-ups can be relocated to allow various swarm configurations. An astronomical source simulator located at a large distance from the mock-ups will provide a source signal for the measurement. Due to the large distance between the transmitting source and the receiving mock-up satellites, the testbed will probably be used outdoors.

1.4 Research objective

The goal of this bachelor's assignment is to continue with the work of Brethouwer performed on the testbed. He was not able to completely finish the testbed and left parts of it up to future work. The intention of this assignment was not directly to complete the testbed, as there is lots of work to be done, but at least complete some parts of it. To support the goal of this bachelor's assignment the following research question was set up:

Research question:
What are the unfinished parts of, and open issues with Brethouwer's design for the OLFAR testbed, and how can the design best be completed and implemented?

1.5 Report organization

The remainder of this report is organized as follows. In Chapter 2, essential theory of radio telescopes is discussed. Next in Chapter 3 an overview of the testbed is given. In Chapter 4 the construction and characterization of the satellite mock-up prototype is documented. Chapter 5 provides some information on changes made to the astronomical source simulator. The receiver implementation is described in Chapter 6. Updates to the software of the testbed are discussed in Chapter 7. Then in Chapter 8 the design for the physical construction is reviewed. Finally the thesis ends with Chapter 9, in which the conclusions of the work during this bachelor's assignment is summarized and recommendations for future work are given.

Chapter 2

Theoretical background

This chapter has been added to provide the reader with some background on the topics discussed in this thesis project. It is recommend that the reader also reads M. F. Brethouwers thesis on the design of the testbed for additional information.

2.1 Principle of interferometry

The challenge in radio astronomy is to get the highest resolution images to see as much details as possible. The resolution determines the smallest size of a feature that can still be identified in the image. The resolution for classical single dish telescopes is limited to the physical size of the aperture. In most cases this is the size of the dish used in the telescope. The resolution of a radio telescope is described by a measure of angular resolution in degrees or radians. A higher resolution means a that a smaller angle can be distinguished. The relation between the angular resolution and the size of the aperture is approximated by the following formula [5]

$$\theta_d \approx \frac{\lambda}{D}, \tag{2.1}$$

where θ_d is the smallest angle, λ the wave length and D the diameter of the aperture.

At some point, building an even larger dish for the radio telescope becomes impossible because of physical construction limits. Therefore, the resolution of a classical radio telescope is limited. This problem is solved by using interferometry, where a larger aperture is synthesized using multiple small antennas in an array. The following sections will give a very simplified explanation of interferometry to provide the reader with a basic understanding of the concept and to explain the choices made for the testbed.

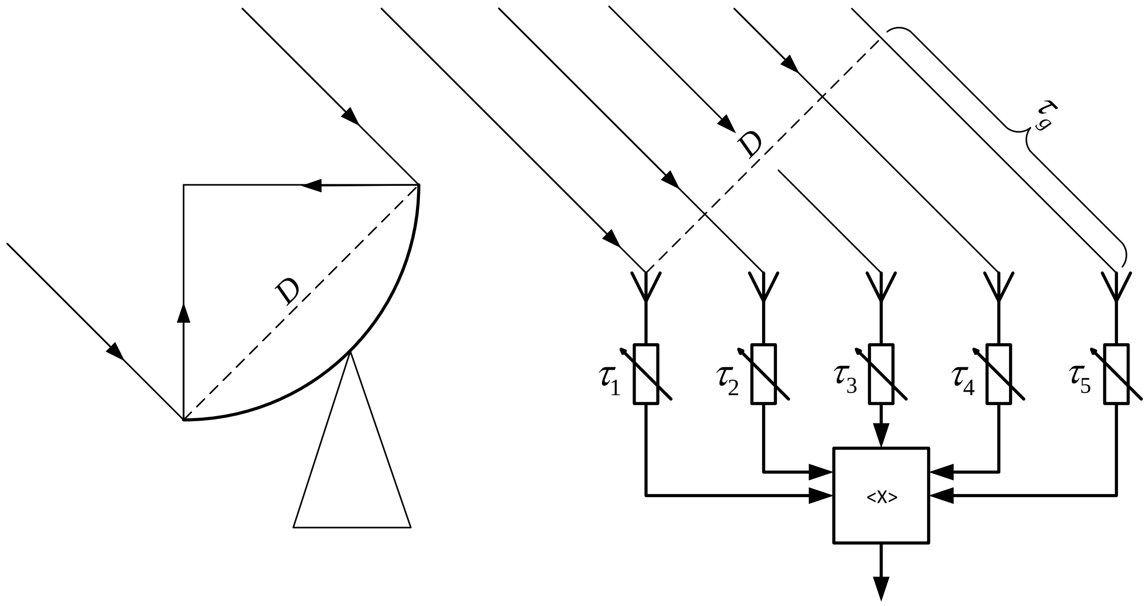

Figure 2.1: Comparison of a classical radio telescope with an antenna array

Figure 2.1 shows a schematic overview on how the larger aperture is created using multiple antennas. The resolution is now not dependent on the apertures of the antennas but on the largest distance between the antennas. This way the resolution can be easily increased by placing the antennas further apart, sometimes to hundreds of kilometers as is the case in Very Long Baseline Interferometry (VLBI).

To be able to compare the signals of the antennas for interferometry the source must be far away so that the incoming wave can be approximated as a plane wave with parallel wave fronts. The incoming plane wave arrives with different time delays on the antennas. When making the narrow-band assumption, stating that the bandwidth of the incoming signal is much lower its carrying frequency, this time delay can then be fully described using only the phase difference of the signals at the antennas.

Individual time delays are added to the antenna signals to steer the beam. This way one can look at one specific direction, this is similar to rotating the dish of the classical radio telescope. When the signals are analysed in the digital domain, one could look at multiple directions simultaneously by applying the different time delays to the received signals, instead of only looking in one direction using fixed delays. Relating the incoming signals to time delays is done using correlation. For simplicity the process of interferometry is explained using a basic interferometer, the interferometer with only two elements.

2.1.1 Two-element interferometer

In the two-element interferometer, two antennas are separated by a baseline distance D. Figure 2.2 shows the two-element interferometer with one incoming plane wave. This plane wave arrives at a the second antenna, a geometric delay of τ_g later than at the first. Of course if there are sources present coming from multiple directions they will all arrive with at antennas 1 and 2 at different time delays. The influences of these sources are added up in the signals of the antennas, and cannot be directly distinguished from each other. The two signals of the two antennas are combined using a correlator, which multiplies the two signals and then integrates the outcome.

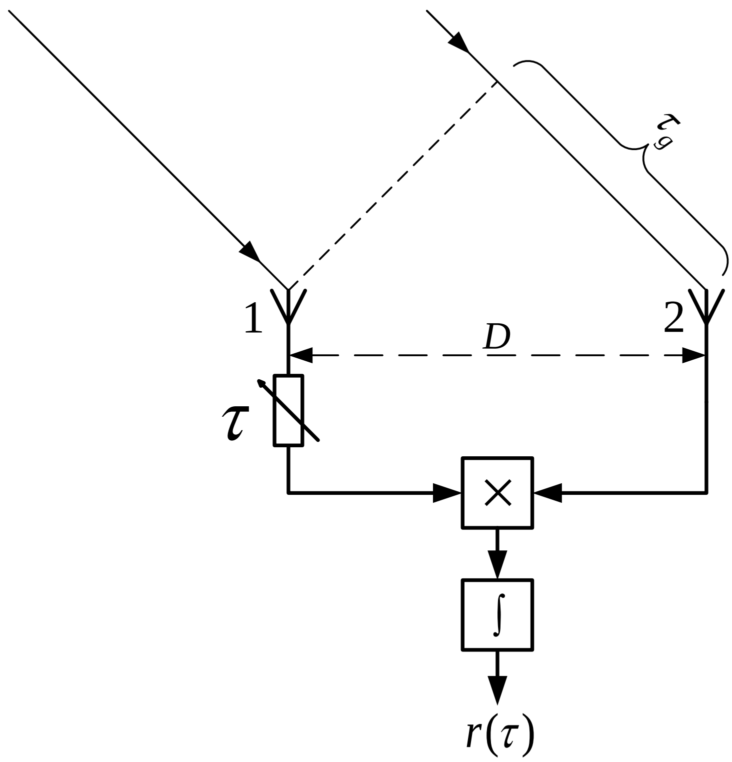

Figure 2.2: The two-element interferometer

The correlation can be described as

$$r(\tau) = \int v_2(t) \cdot v_1^*(t - \tau) dt, \tag{2.2}$$

where $r(\tau)$ is the output of the correlator, $v_2(t)$ the signal of antenna 2 and $v_1(t - \tau)$ the complex conjugate of the signal of antenna 1, time shifted by an instrumental delay τ.

The complete algebraic calculation of this correlation is omitted from this explanation as it is not necessary to understand the basics of interferometry. These can however be found in many texts, e.g. [5]–[7]. One can understand how the interferometry process works by examining Equation 2.2. This equation basically shifts one of the two signals in time by τ and calculates the correspondence over time between these two signals. In other words it gives a measure of correspondence between two time signals with a time difference of τ. If the result of $r(\tau)$ is high for a certain τ this would mean that for this geometric delay the two antennas receive the same signal (have high correspondence). This delay corresponds to a certain angle of incidence or 'position in the sky' of the source. Multiple sources would give multiple delays for which the correlation function is higher.

In most interferometer setups on Earth there is actually no changing instrumental delay used for the correlation process. Instead, the baselines of an interferometry setup are changing because the Earth is rotating. This rotation causes the baselines to change relative to the source allowing the instrumental delay τ to be set constant or even to zero. Because now the same snapshot is taken using different baselines, there are still multiple points of the correlation function $r(\tau)$. In other words there are multiple geometric delays τ_g.

This process of correlation can be extended to more antennas. Each antenna pair would be correlated resulting in a matrix of covariances. The resolution of this interferometry setup is determined by the maximum distance between two antennas, also called the maximum baseline distance. The equation for the angular resolution is similar to that of Equation 2.1 only now it is dependent on the maximum baseline distance and not on the aperture size [5], [8]

$$\theta_d \approx \frac{\lambda}{D_{max}}. \tag{2.3}$$

As was already stated, the distance of the source should be far away so that the incoming wave can be considered as a plane wave across the entire array. This distance D_{source} should satisfy [7]

$$D_{source} >> \frac{D_{max}^2}{\lambda}. \tag{2.4}$$

In Figure 2.3 a situation with two stationary sources is depicted. In this example the radio waves from source A arrive a $\tau_{g,a}$ later at the second antenna compared to first antenna. While the radio waves from the second source B arrive at a $\tau_{g,b}$ later at the second antenna compared to the first antenna.

The waves from the two sources are added on the antennas and will not directly be distinguishable in the signals from the two antennas.

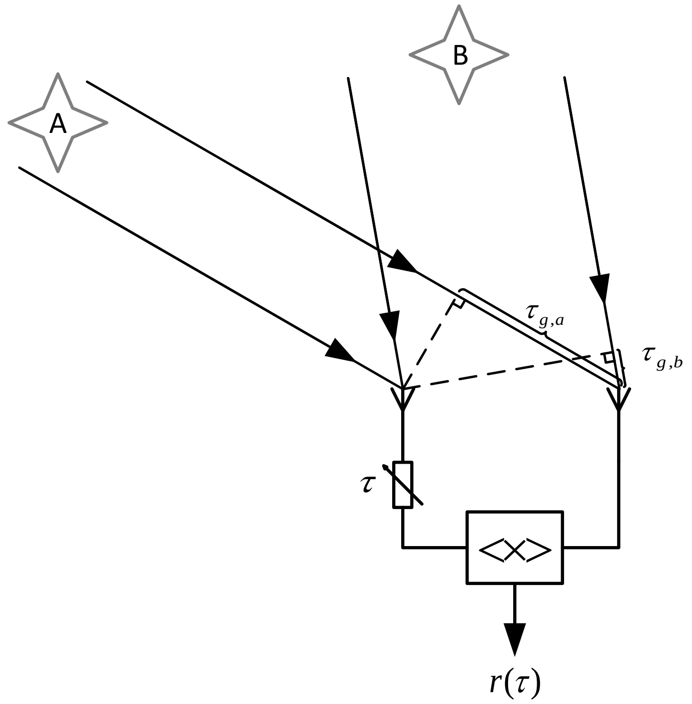

Figure 2.3: Situation with two sources

However, after the correlation function given in Equation 2.2 is applied to the two input signals the output will show two peaks, this is shown in Figure 2.4. The output of the correlation function shows a peak at $\tau = \tau_{g,a}$ corresponding to the first source A, and at $\tau = \tau_{g,b}$ corresponding to the second source B. [1]

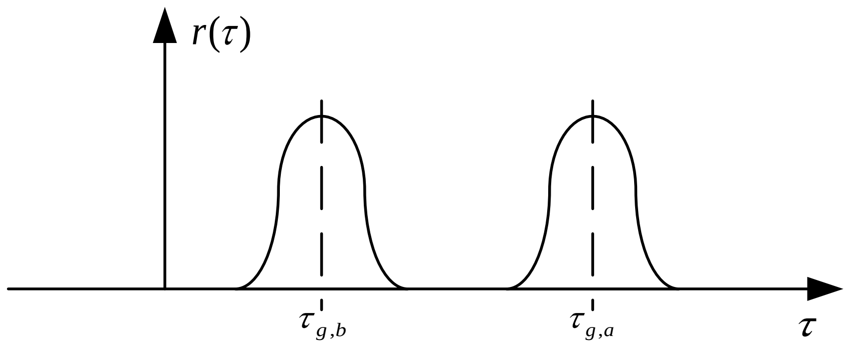

Figure 2.4: Output of correlation function for two present sources

[1] The depicted output of the correlator in Figure 2.4 is actually that of a situation in which the correlated signals are wideband signals. For narrow-band signals, commonly used in interferometry, the output of the correlator would be a sinusoidal with a specific frequency representing the angle of incidence.

2.1.2 Interferometry in OLFAR

The satellites of OLFAR fly in an unstructured 3-dimensional swarm while performing interferometry measurements. Therefore the interferometry setup is more complex than the one presented in the previous section. The principle stays similar to that of the two-element interferometer, where the equation for the angular resolution remains unchanged. However, the equations are extended to three dimensions.

One of the main differences between an ordinary interferometry setup as explained in the previous section and the one in OLFAR is that OLFAR does not use instrumental delays [9]. In OLFAR, each pair of satellites form a baseline distance corresponding to a specific geometric delay for an incoming signal. Because the swarm of OLFAR contains a large number of satellites this results into a lot of different baselines, or delays. A swarm of N satellites would have $\frac{N(N-1)}{2}$ baselines. Therefore it is possible to perform interferometry without adding instrument delays. An additional feature of OLFAR is that because of the orbits of the satellites, their relative positions are constantly changing. This creates a lot of additional measurements with different baselines. When the measurement results of all these different configurations are combined this will result in an even clearer image.

Creating images from the interferometry measurements is an extensive tasks that requires multiple measurements to be stored and combined. Therefore the satellites only correlate their signals with each other and send it back to an base station on Earth with their individual position and orientation data. The base station then calibrates the data and post-processes it to generate the fish-eye images.

2.1.3 Consequences for the testbed

In the previous sections the general concept behind interferometry and how it is used in OLFAR was explained. As was shown in these sections, the principle of interferometry is based upon the time difference in signals measured at different antennas caused by the geometric delays.

Because delays are measured in the interferometry process three factors are of importance for the testbed. These three factors are manifested in various aspects of the design and operation of the testbed. First, to get accurate delay measurements accurate baselines are required. The testbed should therefore provide accurate and stable placement of the observing antennas. If the relative distances between antennas are not precisely known or vary due to instabilities in the physical construction, it will result in inaccuracies in the interferometry process.

Secondly, there are several points of the testbed that may introduce signal path delays. For example, a different length in the feed lines running from the observing antennas to the receivers might cause an additional unforeseen delay. These delays can be calibrated, but should be known beforehand

Finally, the precision of the clock synchronisation in the receivers determines a large part of the accuracy of the testbed. If two clocks signals are lagging with only a nano second the baseline would be 30 cm shorter than it actually is. When the baseline is not accurate, the interferometry process will show inaccuracies.

All of the design specifications and requirements presented in this thesis and that of Brethouwer are set up with the above considerations in mind to ensure that the testbed is stable and accurate enough to perform the interferometry.

Chapter 3

Testbed overview

The aim of this chapter is to give a brief overview of the design of the complete testbed. In the chapters following this chapter, the specific components of the testbed are examined in more detail.

3.1 Specifications and boundary conditions

Brethouwer already set-up a big part of the specifications and boundary conditions for the design of the testbed. These specifications are based on the specifications of OLFAR, but do not necessarily match the specifications of OLFAR. Some specifications are scaled to the size of the testbed as for example the operating frequency range. A summary of the specifications of OLFAR, which are relevant for the testbed, was created by Brethouwer provided in Appendix A [4, App. A]. Below the specifications and boundary conditions for the testbed are summarized. More detailed specifications can be found in the chapters for each component of the testbed.

- Radio interferometry setup with a maxium baseline distance of 1.17 m
- Reconfigurable antenna system representing OLFAR's satellite constellation
- Controllable via a computer running MATLAB
- Legal operation in the 1271 - 1272 MHZ and 1294 - 1295 MHz bands
- Setup which is portable by car or trailer
- Affordable setup

3.2 Functional design

As mentioned in the previous section, the testbed is aimed to represent the specifications of OLFAR but is not completely identical. This section will discuss the differences between the testbed and OLFAR in more detail and shall give an overview of the five components the testbed can be divided into.

A diagram of the functional design of the testbed can be seen Figure 3.1. The testbed has a signal source that transmits the signal of representing an astronomical source. This can be seen on the left side of Figure 3.1. The signal will be received by five satellite mock-ups. Each mock-up has three antennas and receives, similar to the satellites in OLFAR. These are shown in the middle of Figure 3.1. Commercially off the shelf software defined radios (SDRs) are used for the receivers. These receivers are programmable by software which ensures flexibility of the testbed. As in OLFAR the receivers inside a satellite share the same clock signal (indicated with the red lines). The groups of receivers are also synchronised ensuring that they start measuring at the same instance (indicated with the green lines). The receivers are controlled on a computer running MATLAB, shown on the right of Figure 3.1. This computer also stores the individual data streams with antenna signals coming from the receivers (indicated by the blue lines) and performs the correlation of these signals.

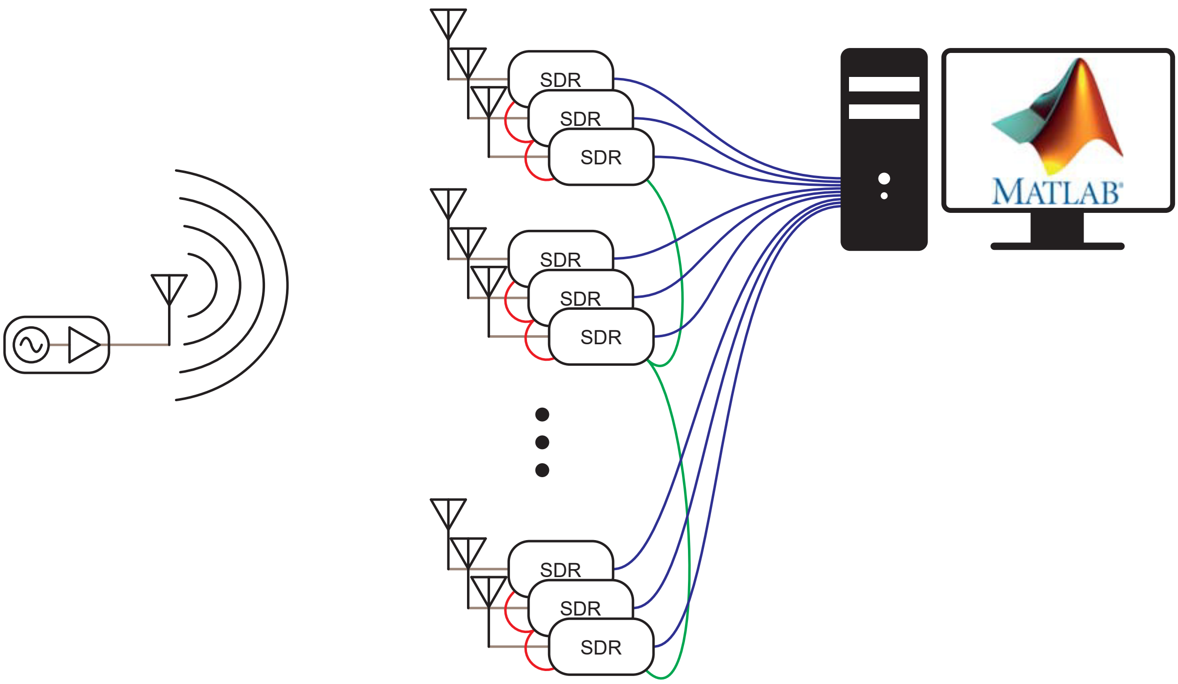

Figure 3.1: Function Diagram of the testbed

To scale down the size of the testbed it will operate in a higher frequency range than OLFAR. This scaling will allow the testbed to be portable without it having a considerable consequence on its usability for testing the algorithms for calibration and RFI mitigation. Brethouwer already chose two frequency bands for the testbed to operate in, the 1271-1272 MHz band and the 1294-1295 MHz band. For calculations the frequency which lies in the center of the two bands of 1283 MHz is used, this results in a wavelength λ equal to 0.2337 m. The maximum baseline distance, as explained in Section 2.1, is chosen to be 5λ equal to 1.17 m. Using these two values the other properties of the interferometry setup can be determined using Equation 2.3 and Equation 2.4. These are shown in Table 3.1.

Table 3.1: Interferometry specifications

Center frequency	f_o	$1283\ MHz$
Wavelength	λ	$0.2337\ m$
Maximum baseline distance	D_{max}	5λ or $1.17\ m$
Angular resolution	θ_d	$0.20\ rad$ or $11.5°$
Source distance separation	D_{source}	$>>\ 5.84\ m$

3.2.1 Components of the testbed

The testbed can be divided into five seperate components, the Astronomical Source Simulator, the Observational Antenna System, the Software and the Physical construction. The next sub-sections will give a short description of each component. The components are discussed in more detail in the following chapters.

Observational antenna system

The measurement antennas of OLFAR are three orthogonal active short antennas [10]. The system is active with a high input impedance receivers to also be able to measure the low-frequencies. Because of the higher operating frequency of the testbed, the antennas do not have to be as big as the ones in OLFAR. In the testbed the satellites are replaced by satellite mock-ups, each containing three orthogonal dipole antennas which are not short antennas but just half wavelength dipoles. The antennas have a output impedance of 50 Ω which matches the input impedance of the receivers and cables.

Astronomical source simulator

The Astronomical source simulator is a source that transmits radio waves that represent the radio waves transmitted by an astronomical source. It produces the source signal for the testbed as shown on the left of Figure 3.1 that is used as a calibration point for the algorithms. The Astronomical source simulator consists of two parts, the source antenna and the source generator.

Receivers

Instead of using an active antenna system with high input impedance receivers as in OLFAR, the testbed will use a system with standard 50 Ω output and input impedances. The receivers will be commercially off-the-shelf (COTS) SDRs that are capable of clock synchronisation. The capability of clock synchronisation is essential to mimic the properties of OLFAR. As OLFAR is a distributed radio interferometry telescope, the receivers cannot just run off a single clocks. A special clock distribution system is implemented which will also be represented in the testbed. Chapter 6 will discuss this synchronisation system in more detail.

Software

The software of the testbed controls the various functions of the testbed. As the receivers are SDRs, a lot of functionality is implemented using software. This concerns the communication between the receivers and the computer as well as the execution of a measurement cycle, the acquisition, storage and processing of the measurement data. The testbed will be operated by a computer running a MATLAB script. The usage of MATLAB allows for the data to be directly processed in the calibration and RFI mitigation algorithms.

Physical construction

The physical construction of the testbed concerns all the parts that are needed to hold the previous components in place. Most importantly it should ensure that the measurements taken with the testbed are accurate and repeatable. It will also determine the flexibility in the placement of the satellite mock-ups. The physical construction should allow for various satellite constellations while keeping an accurate placement of the mock-up. It should therefore ensure stability to keep the measurements repeatable.

Chapter 4

Observational antenna system

M. F. Brethouwer designed an Observational antenna system to be used in the testbed. His design consists of three orthogonal antennas, representing the antennas of OLFAR, mounted on top of a pole. He then verified the performance of the designed antenna using simulations. These simulations showed that the antenna pattern of each of the orthogonal half wave dipoles only had a 3% difference in the antenna pattern compared to that of an ideal dipole [4]. This difference is caused by the influence of additional elements close to the dipole such as feed-lines and the two other dipoles.

During this bachelors's thesis project a prototype of Brethouwers design for the Observational antenna system was constructed and characterized in experiments. First a set of specifications for the Observational antenna system are given which were set up by Brethouwer. In following sections, a brief summary on the construction prototype is given, after which the different experiments for characterizations are discussed

4.1 Specifications

The specifications of the Observational Antennas were already set up by Brethouwer so that they could represent the low frequency antennas of OLFAR [2], [4]:

- Three orthogonal antennas
- Antenna phase centers close together
- Linear polarized antennas
- Omnidirectional dipole-like antenna patterns
- Center frequency of 1283 MHz
- Similar antenna patterns for each antenna
- 50 Ω output impedances

4.2 Design and construction

Brethouwers thesis contained a complete design for an antenna system with three orthogonal antennas on top of a PVC pipe. Some changes were made to the design of Brethouwer to allow easier construction. The final design can be seen in Figure 4.1a. This design has been inspired by the patent of a field probe antenna [11]. Each Observational Antenna has three orthogonal dipoles. The dipoles are each mounted on printed circuit boards (PCBs) and are angled $54.7°$ with respect to the vertical feed line. This angle ensures that the influence of the feed lines on all three antennas are equal [4, Ch. 5.2].

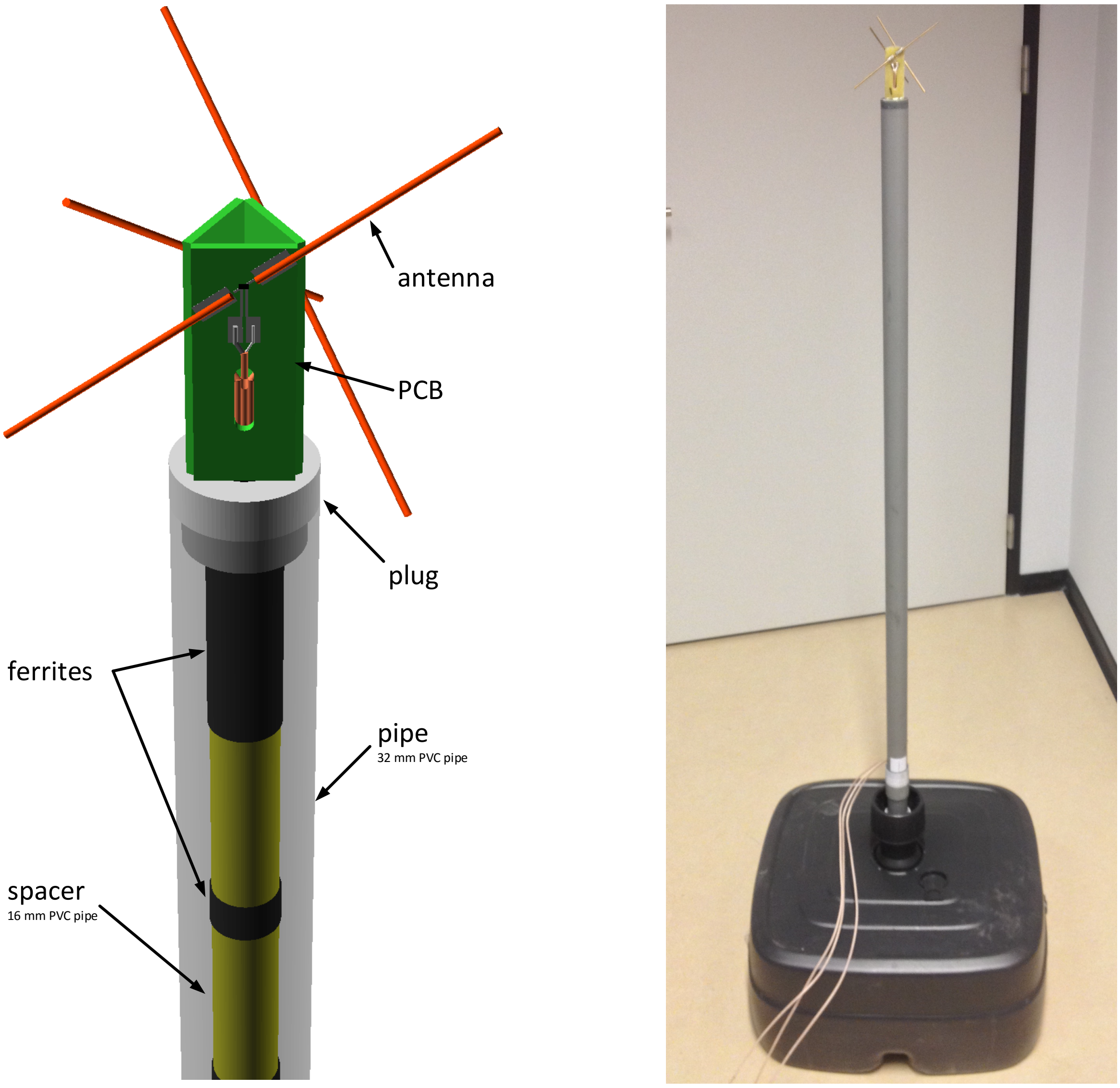

(a) Final design *(b)* Prototype

Figure 4.1: The designed and constructed prototype

A complete documentation of the changes made in the design and the construction process of the Observational antenna prototype is given in Appendix B. The constructed prototype can be seen in Figure 4.1b, more pictures can also be found in the appendix. In this section the interesting design choices are highlighted and discussed.

The three antenna PCB are mounted on top of a 1 m high PVC pipe. This length is chosen because it lies in between the minimum height of about 50 cm and maximum height of 1.75 where the antennas may be placed. The minimum height set so that the antennas are not too close to the feed lines or the ground while the maximum height ensures that two antennas do not differ more than the maximum baseline distance in height.

The three feed lines, one for each antenna, run from the PCBs through the center of the pole to the bottom. Every 6 cm (quarter wavelength) there is a ferrite core placed on the feed lines to suppress common mode currents. If common mode currents start to flow on the feed lines those feed lines will start to act as antennas as well. This effect is unwanted because it distorts the radiation patterns of the dipoles. The ferrites are spaced using PVC pipes that are regularly used for electrical installations. The first 6 cm of the feed lines are completely filled with ferrites to further suppress common mode currents. Filling the top of the feed lines with ferrites proved to give a significant improvement in suppressing the common mode currents as showed in simulations by Brethouwer [4, Ch. 5.3].

The type of PCB material was chosen to be standard FR-4. This material has a dielectric constant or relative permittivity of around 4.7 [12], meaning it has a absolute permittivity of almost 5 times higher than vacuum. This higher permittivity could influence the radiation patterns, however the choice was made to still use FR-4 and see how much influence it has. If the FR-4 material proves to be too influential it can always be replaced with a material designed for RF applications such as I-Tera MT RF, which has a lower relative permittivity of around 3.5 [13].

Instead of using copper rods for the antenna dipoles, 3 mm brass rods were used because these were available at the self service workshop. Brass has a higher resistivity than copper, however it is probably still low enough for the brass rods to be used as antennas. If the brass dipoles prove to be unsuitable for the testbed they could always be replaced by copper rods.

Some recommendations for the design and construction of the other Observational antenna systems are given in Appendix B. This appendix should provide, together with the 3D models on the USB provided with this theses, enough information for building multiple Observational antenna systems.

4.3 Characterization

After the prototype had been constructed it was to be characterized in a set of experiments. These experiments were aimed to find if the designed antenna meets the specifications stated in Section 4.1. The goal of these experiments is formulated in the following research question:

Experiment research question:
How do the characteristics of the dipoles in the Observational Antenna prototype correspond to ideal dipoles and are they suited for usage in the OLFAR testbed?

Brethouwer ran extensive simulations to verify the design of the Observational Antenna prototype. Those simulations showed an expected dipole like behaviour of the antennas [4]. A reasonable hypothesis would therefore be to expect that the prototype will at least show similar behaviour to the simulations. The performance of the antenna will mostly depend on whether or not the ferrites om the feed lines suppress common mode currents in the feed lines.

The following three sections will discuss the experiments conducted to characterize the antenna prototype. The first experiment looks at the output impedance of the three dipoles in the antenna prototype. The second experiment is aimed to find the radiation pattern of each of the three dipoles. In the third experiment the polarization of one of the three dipoles is measured. In a fourth section following the experiments the influences of the anechoic chamber on the measurements are examined. Some background on antenna measurements can be found in Chapter 11 of the book *"Antenna Theory Analysis and Design"* by C. A. Balanis [14].

4.3.1 Output impedance and center frequency

The output impedance of the antenna is essential for matching the antenna on the input impedance of the receivers. A mismatch would result into power being lost, which is detrimental to the performance of the testbed. The output impedance of an antenna is usually specified as the voltage standing wave ratio (VSWR) at a specific frequency. For the testbed this frequency is equal to the center frequency at which the testbed operates, namely 1283 MHz. The receiver and cables in the testbed have an impedance of 50 Ω. For perfect matching the output impedance of the antenna should therefore also be 50 Ω at 1283 MHz. The 1:2 balun on the antenna PCBs makes sure that the dipoles are matched to the cable, however this matching is not perfect. The accuracy of the matching is determined by how close the VSWR is to 1.

Method

As shown in Appendix D the VSWR can be easily determined from the S22 parameter. This parameter can be found using a vector network analyser (VNA) in an 1-port or 2-port measurement. For this experiment the Agilent Technologies N5230A VNA was used to measure the S-parameters. This VNA has a 50 Ω input impedance just like the receivers that will be used in the testbed.

After a 2-port calibration to compensate for the reflections of the cables the antenna prototype was connected to port 2 of the VNA. An off the shelf 1 - 4 GHz horn antenna was attached to port 1 of the VNA but was not used during this experiment. The observed spectrum spanned a frequency range of 1.5 GHz centred around the carrying frequency of 1.283 GHz. The total of measurement points in the frequency span was set to 801 resulting in a measurement step of 1.8750 MHz. When measuring one of the three antennas the other two were terminated with a 50 Ω load.

To minimize external RFI and reflections the measurements for the characterization of the observational antenna prototype were conducted in an anechoic chamber. Figure 4.2b shows the prototype standing on its base inside the anechoic chamber. The horn and the prototype were placed in opposite corners of the anechoic

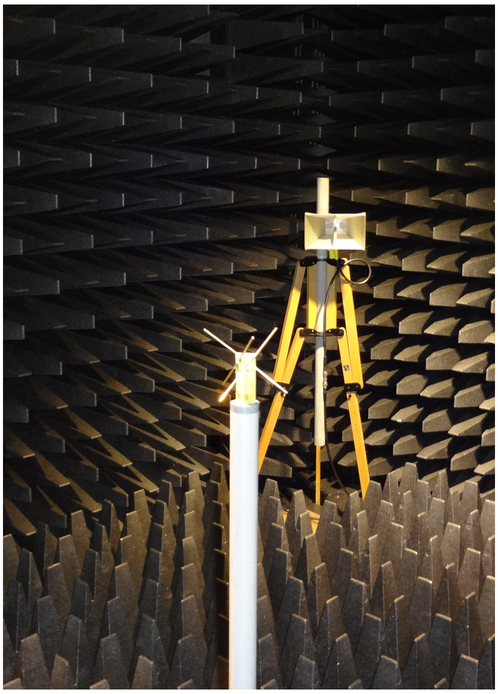

(a) Transmit and recieve antenna are placed diagonally in chamber

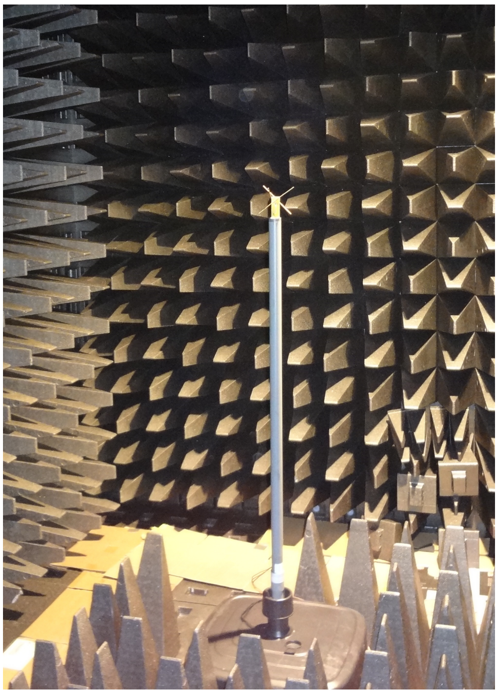

(b) Prototype placed in corner

Figure 4.2: Antenna setup in anechoic chamber

chamber to make sure that any reflecting waves from the walls behind the antennas are not reflected back to the antenna. This reduces the reflections to mainly those coming from the ceiling and floor of the chamber. Figure 4.2 shows the setup in the anechoic chamber.

Results

Figure 4.3 shows the measured S22 parameter of the three antennas over frequency. Only the magnitude of the S22 parameter is plotted. For completion the phase of the S22 parameter should also be plotted, but these were omitted because they are not of importance for this experiment. In each plot the S22 parameter of a single antenna PCB with a short cable ($<$5 cm) was added for comparison. From the measured data the VSWR and return loss of each antenna in the prototype were calculated using Equation D.3 and Equation D.4 respectively given in Appendix D. The calculated values can be found in Table 4.1.

All the measurements of all three traces lie below -7 dB which suggests that there are some resistive losses. These are possible due to the cables and the losses of the balun. In the measurement with a short cable directly to an antenna PCB these losses were notably less, about -2 dB. The magnitude traces of all the three dipoles show a clear ripple across the frequency span. This ripple is created by the output cable of the antenna as this one is not calibrated in the 2-port calibration. This was validated by doing a similar measurement with a long cable attached to an antenna PCB. In this measurement the ripple was clearly shown while in the measurement with a short cable the ripple was not present.

Noticeably, antennas II and III show a dip in magnitude around 750 MHz while antenna I and the dipole with a short cable only show a small decrease in magnitude. The antenna did not seem to transmit/receive at this frequency as the S21 and S12 parameters did not show an increase in power at this frequency. The cables from the three antennas are of the same length and are therefore not a probable cause of this dip. If this dip was due to the cables it should also have shown up in the trace of the first antenna. This dip is unlikely to influence the performance of the antenna in the testbed because the antennas will not operate in this frequency range.

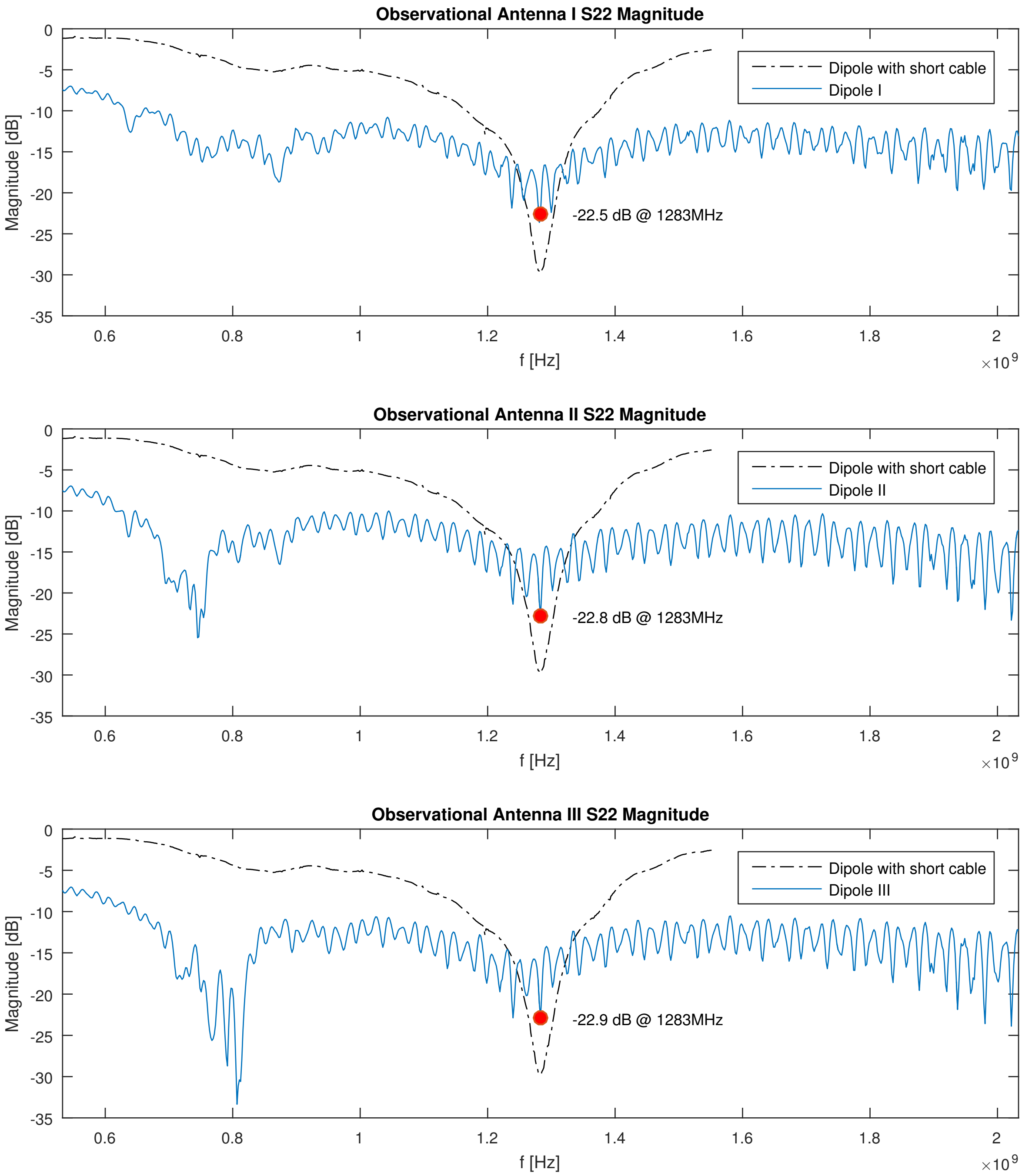

Figure 4.3: S22 magnitudes of three dipoles

Table 4.1: Standing wave ratio's and return losses for the prototype at 1283 MHz

Dipole	VSWR	Return Loss [dB]	Return Loss [%]
1	1.1618	22.5153	0.56
2	1.1561	22.8057	0.52
3	1.1542	22.9027	0.51

Brethouwer simulated the VSWR for various lengths of the dipoles. In his simulation the optimal length of 5.5 cm for each of the two rods of the dipole gave a VSWR of 1.35 [4, Ch. 5]. The reason for the difference with the measurement is that the measurement does not take into account the resistive losses in the feed lines. These resistive losses can be approximated by taking the difference in the S22 parameter between the dipole with a short cable and the Observational antenna dipoles, this is about 5 dB. This loss appears twice for the reflected wave and should be added to S22 value to find the actual VSWRs and return losses. Table 4.2 shows the VSWR and return losses taking into account the resistive losses. The remaining differences might be due to the losses and reflections appearing at the balun.

Table 4.2: Standing wave ratio's and return losses for the prototype at 1283 MHz taking resistive losses into account

Dipole	VSWR	Return Loss [dB]	Return Loss [%]
1	1.6203	12.5153	5.6
2	1.5938	12.8057	5.2
3	1.5553	12.9027	5.1

From the experiment it can be concluded that the antennas operate according to the specifications. All three antennas have a VSWR of around 1.6:1 as shown in 4.2 resulting in a return loss of around 5 %. This means the antennas are reasonably matched to 50 Ω. The S22 traces also shows that the antennas have a dip at 1283 MHz, allowing them to operate at the center frequency of the testbed. This means that the fifth and seventh specification, center frequency and output impedance, given in section 4.1 are satisfied.

4.3.2 Radiation pattern

An important characteristic of an antenna is its radiation pattern, as it determines in which direction the antenna can receive. The satellites in OLFAR use a similar antenna setup with three orthogonal dipoles. The pattern of these three dipoles together form an omnidirectional receiving pattern. For the testbed the three dipoles should also create a omnidirectional antenna pattern allowing the observational antenna system to receive from every direction. For interferometry it is important that the antenna pattern of each individual dipole is smooth and predictable. If this is not the case, it is not possible to determine if a bright spot in the image is created by a source or because the antenna has more gain in that particular direction. For the radiation pattern both the horizontal and vertical polarization are measured.

Method

The setup to measure the radiation pattern was similar to the setup used in the previous experiment. However, this time the horn antenna is used to transmit a linearly polarized wave. Figure 4.2 shows a schematic drawing of the used setup. The VNA was set to the same settings as in the previous experiment having the horn connected to port 1 and transmitting a wave while one of the dipoles of the antenna prototype is connected to port 2.

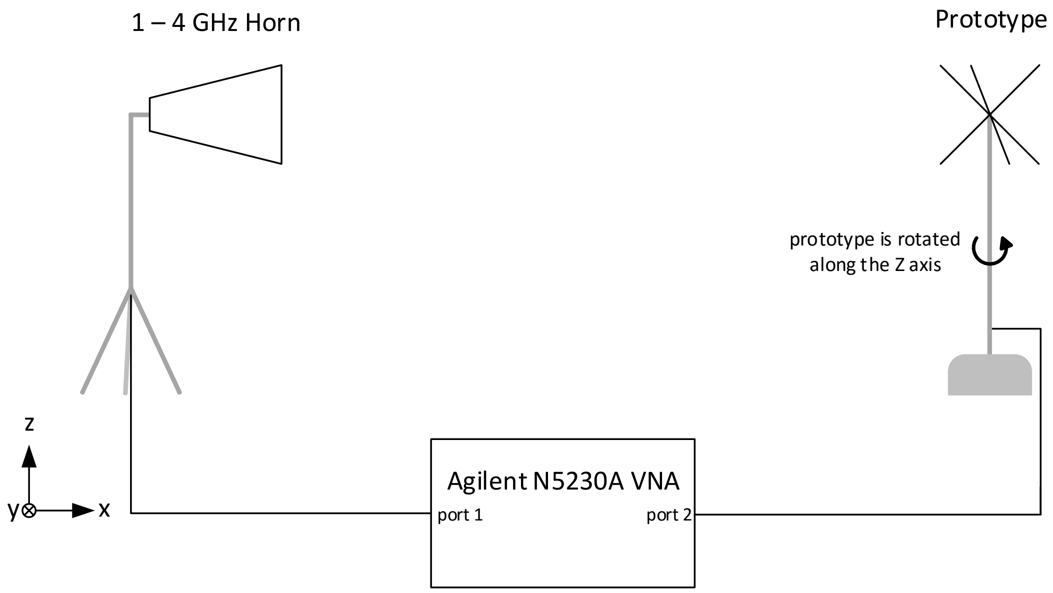

Figure 4.4: Setup for measuring the antenna radiation pattern

During a measurement of one dipole the output cables of the other two were terminated with a 50 Ω load. The S-parameter that is now of interest is S12, the reverse voltage gain. This parameter represents the ratio between the transmitted wave and received wave. The S21 parameter could also been used for this experiment, because all elements in the system are passive and the system is reciprocal. The S21 is therefore equal to the S12 parameter.

To measure the radiation pattern of an antenna either the source has to be rotated around the antenna under test or the antenna under test has to be rotated itself. For this experiment it was chosen to rotate the prototype antenna as it is easier to ensure that the distance between the antennas stays the same during the measurements. The radiation pattern was only observed in the horizontal azimuthal plane because measuring in the elevation plane would require a setup that allowed for different height positions of the transmit antenna or tilting of the antenna prototype which was not available. However, when the testbed is operating the source antenna would be at a big distance from the observational antenna system. To then create a difference in inclination the transmit antenna would have to be at a great height which is physically difficult to do. Therefore only the azimuthal radiation pattern is of real interest.

Because of time constrains a manual approach was taken to rotate the antenna. The antenna was therefore rotated by hand as writing software for controlling a stepper motor and automating the measurement would have taken a lot of time. A degree scale was added to the base of the antenna which can be seen in 4.5.

Figure 4.5: Angle scale on base of antenna prototype

The distance between the horn antenna and the prototype was 2.52±0.10 m. At this distance both antennas are separated far enough to be in each others far-field. A total of 36 measurement points were taken, resulting in an angle resolution of 10°. The measurement was conducted twice for each of the three antenna dipoles, once for the horizontal polarization and once for the vertical polarization. Both the horizontal and vertical polarization were taken relative to the ground and not relative to the angle of the dipoles.

Results

Figure 4.6 shows the horizontal polarized measurements of the antenna prototype. For the horizontal polarization the antennas show a clear dipole like pattern with two lobes, however there is a clear difference between the sizes of the lobes. The dipoles have a clear front and backside, having a bigger front lobe than back lobe.

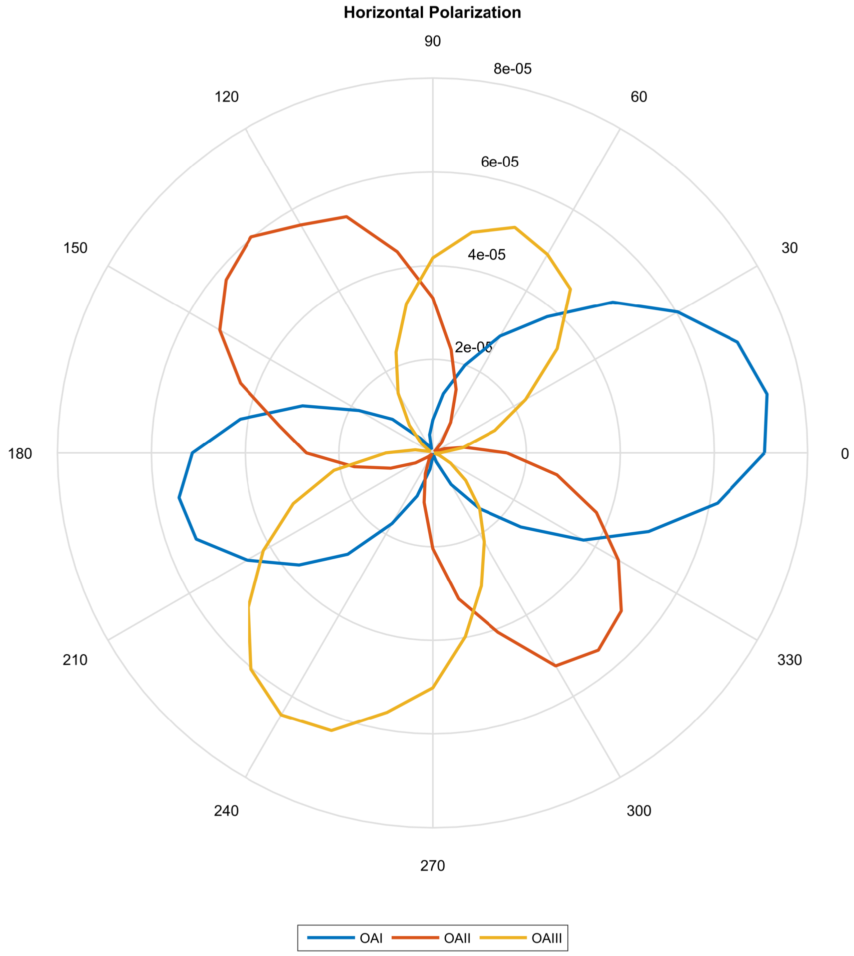

Figure 4.6: Radiation patterns in azimuthal plane of prototype antenna for horizontal polarization

This is however expected as the backside of each antenna is obstructed by three PCBs and two dipoles. The mutual difference in the maximum of the front lobes of the dipoles are about 1 dB.

Figure 4.7 shows the vertical polarized measurements. For this polarization the patterns are clearly more distorted. This is probably due to the fact that for the vertical polarization the antenna pole lies in parallel with the polarization. Resulting in a greater influence of the feed lines on the antenna pattern. The vertical pattern also shows a difference between the front and backside gains for each antenna. This time however the backside shows a higher gain than the front side. This difference might be explained by the influence of the small piece of coax that is at the back side of the PCBs that is not covered in ferrites. In the vertical polarization this piece will influence the pattern more if the backside of the antenna is pointed towards the source.

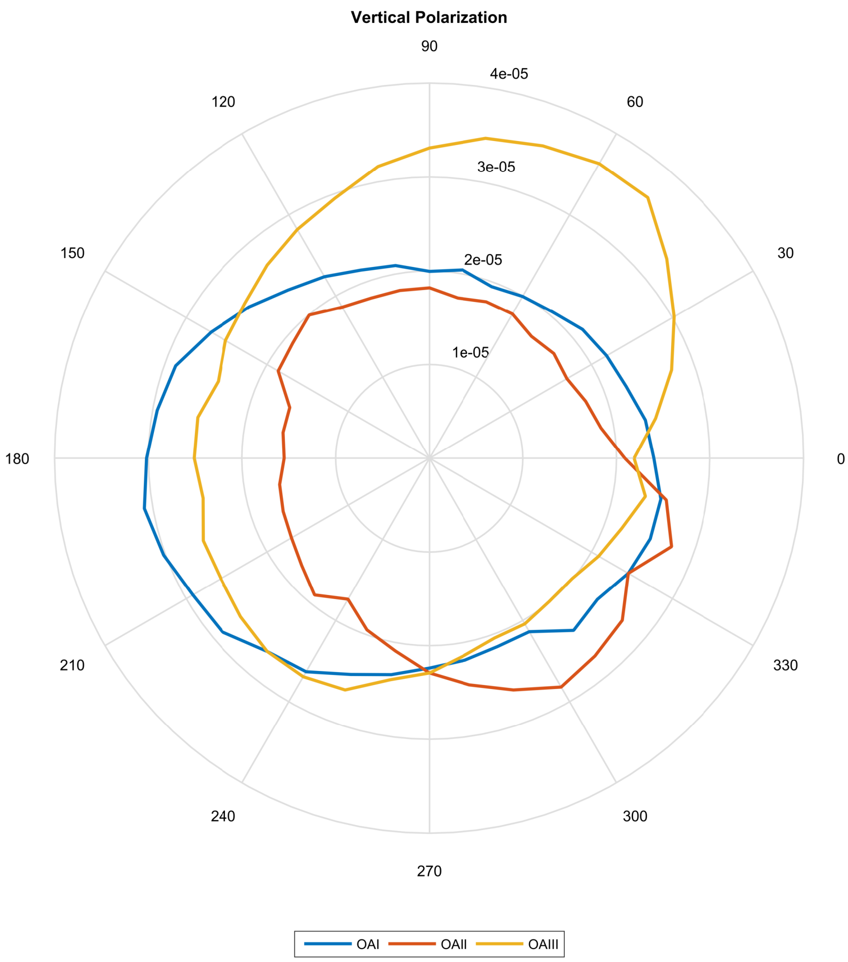

Figure 4.7: Radiation patterns in azimuthal plane of prototype antenna for vertical polarization

The second dipole shows an overall lower gain in its antenna pattern than the other two antennas. The reason for this remains unknown, after repeating the measurement the gain of this second dipole still remained lower than the other two. A possible culprit might be the balun, this could have been broken during the soldering. However because to the hot air soldering iron being broken it was not possible to repair this too see if this is the cause. As this antenna is also performing less in the horizontal polarization the possibility that something is wrong in the balun is likely.

In Figure 4.8 the horizontal polarization measurements are compared to a simulation of an ideal dipole. The simulated pattern has been scaled in such a way that its maximum corresponds to the average maximum of the three dipoles. The measurement shows that the dipoles minima do not lie exactly at opposites sides.

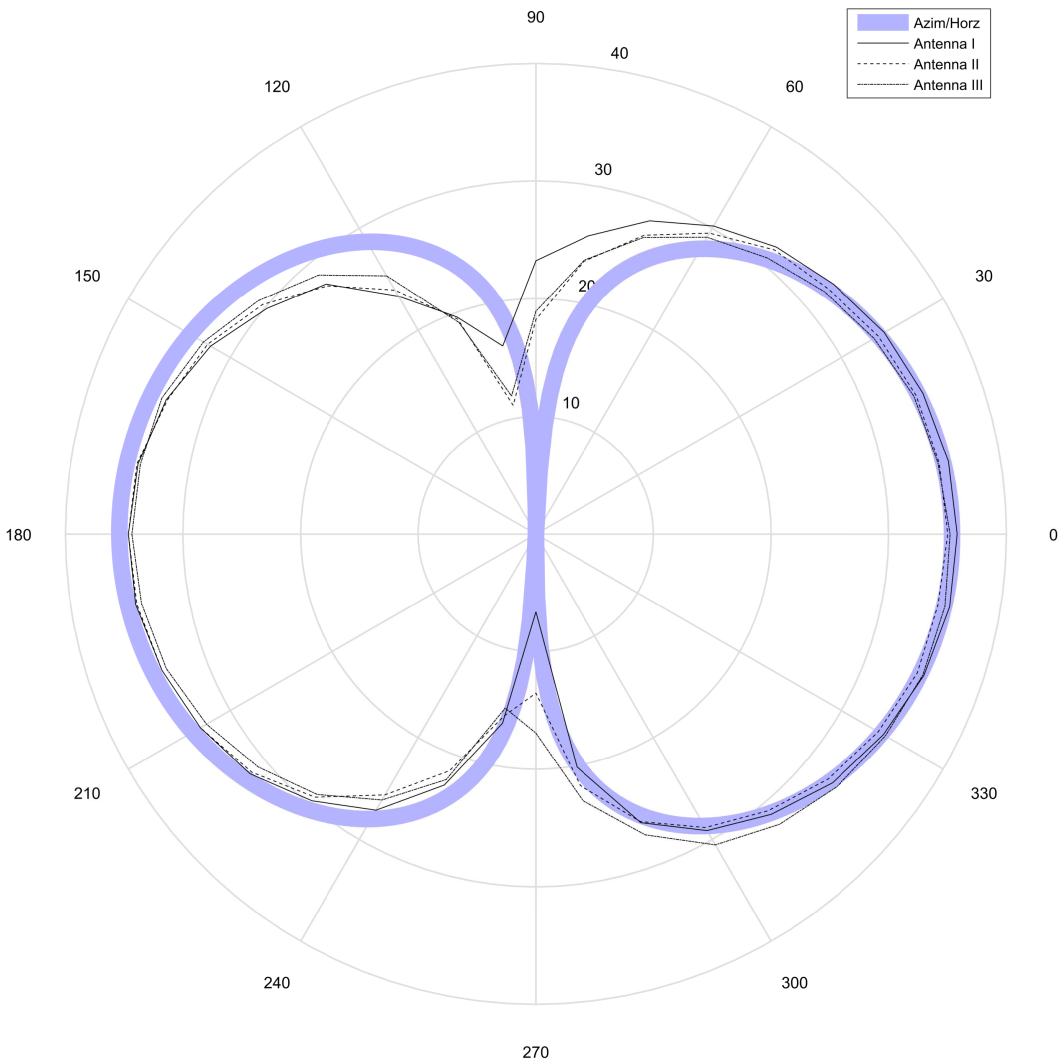

Figure 4.8: Radiation measurements in dB scale compared to an ideal model for horizontal polarization

This might have two reasons. The first one being that while measuring close to the minima of each pattern the measured value fluctuated strongly, sometimes with a few dB. This results in a bigger measurement error for the measurements close to the minima. The second reason is that there are on the back side of each antenna three PCBs and two other dipoles. These elements might cause the pattern to be 'pulled' backwards a bit.

Figure 4.9 shows a comparison between the vertical polarization measurements and a simulation of an ideal dipole. Again the simulated pattern is scaled in such a way that the maximum corresponds to the average maximum of the three antenna dipoles. The vertical patterns show an oval shape just as in the simulation.

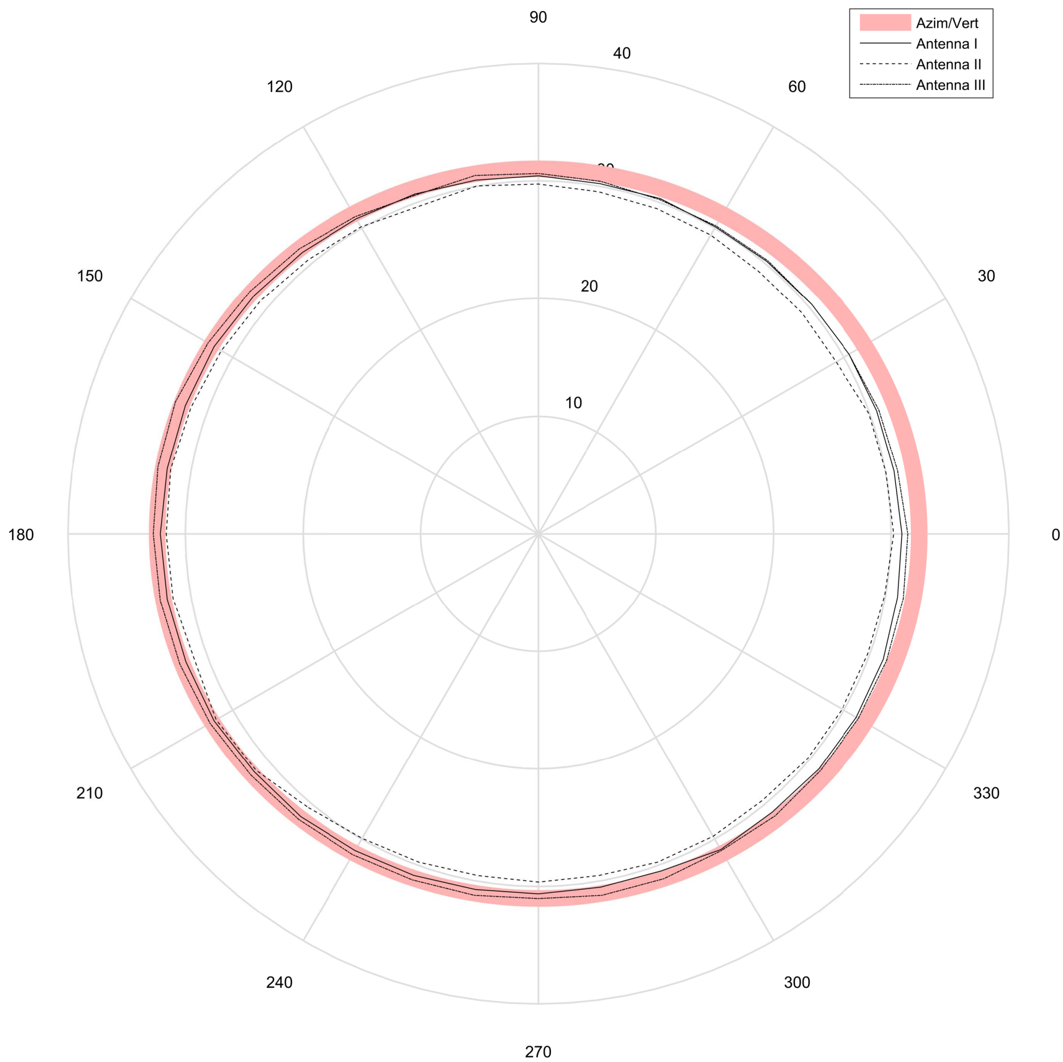

Figure 4.9: Radiation measurements in dB scale compared to an ideal model for vertical polarization

4.3.3 Polarization

The final experiment was conducted to verify if and how strongly the antennas are polarized. Ideally a dipole antenna is linearly polarized, as the dipoles in the antenna prototype are angled 35.3° this would mean that at this angle the gain should be maximum while at an angle perpendicular to 35.3° it should be at a minimum.

Method

For this experiment the same setup as the previous two experiments was used however this time the transmitting horn antenna was rotated around its axis for several measurement points. Figure 4.10 shows the degree scale used on the horn antenna.

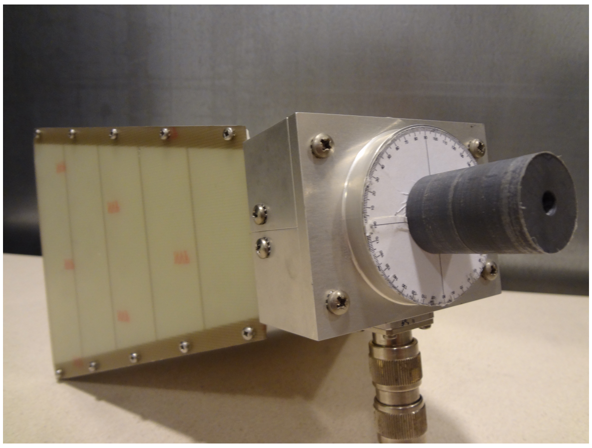

Figure 4.10: Angle scale on horn antenna

A total of 18 measurement points were taken resulting in an angular resolution of 20°. Only a measurement of the first antenna was done because the previous experiments showed similar results across the three antennas. So it is almost certain that also this measurement will show similar results across the three antennas.

Results

Figure 4.11 shows that the antenna is indeed strongly linearly polarized with its maximum around 30°. To be sure the antenna has maximum gain when the angle is 35.3° a measurement with more points should be conducted. However after this experiment the conclusion could already be made stating that the antenna is linearly polarized and therefore meeting the third specification given in 4.1.

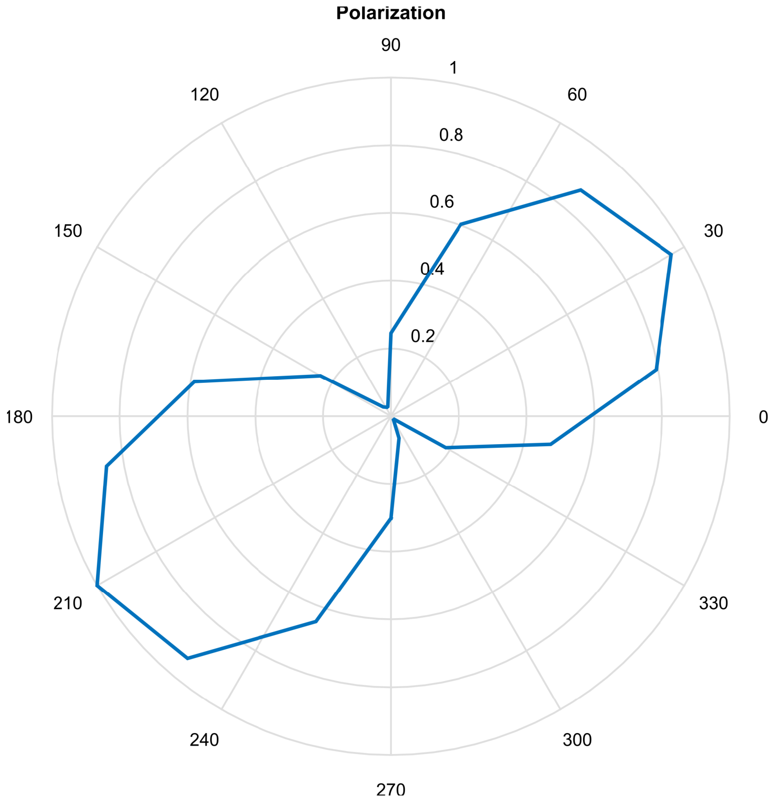

Figure 4.11: Polarization measurement on first antenna

4.3.4 Influence of reflections in anechoic chamber

The anechoic chamber used in the experiments has just recently been installed at the Telecommunication Engineering group on the University of Twente. As the characterization of this antenna was one of the first such experiment done in this chamber there was a lot of interest into how reflections in the chamber influenced the measurement. To answer this question the data gathered during these experiments were examined to find these influences.

Inverse Fourier Transform of transfer

To get a time delay profile of the signal measured at the input of the VNA, the inverse Fourier transform (IFT) of the measured S21 can be taken. The resulting time signal, or delay profile, indicates when signals arrive at the input of the VNA. This delay will show a peak occurring once the direct line of sight wave, transmitted by the transmitting antenna, is received at the receiving antenna. Possible reflections will also show up as peaks, but later in time than the peak created by the direct line of sight wave.

Using MATLAB the IFT of the S21 measurement was taken, the result is the time signal shown in the second graph of figure 4.12. The delay profile shows a clear pulse followed by a second pulse 10ns later. This second pulse is most likely a reflection from the chamber. In the third graph the time signal has been plotted on dB scale. From this plot it can been seen that the difference between the signal strength of the direct line of sight wave and the reflection is about 25 dB.

In conclusion; in this setup the reflected wave from the transmitting horn to the receiving antenna prototype is 25 dB or about 320 times weaker than the direct line of sight wave.

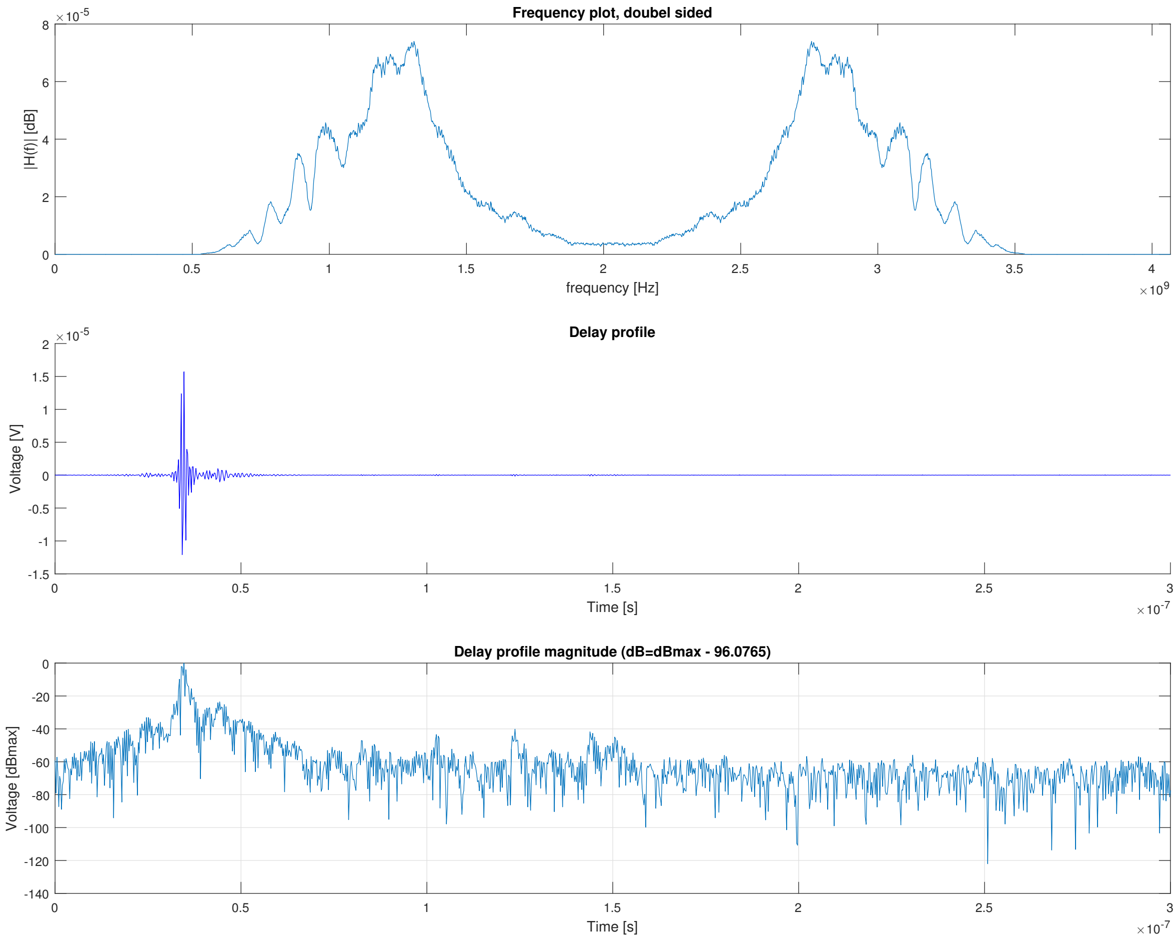

Figure 4.12: Measurement data inverse Fourier transformed to produce delay profile. The delay profile is zoomed in to show $0 < t < 3.0e-7$

To clearly see the influence of the reflections on the measurement the time signal can be windowed to just encapsulate the direct line of sight pulse after which it can be Fourier transformed back to the frequency domain. The result is a frequency spectrum with only the frequency components coming from the direct line of sight pulse. Figure 4.13 shows this time windowed signal and its Fourier transform with the original Fourier transform.

In the lower plot figure 4.13 the influences of reflections are visible. The frequency spectrum of the time windowed pulse shows a smooth line instead of a strongly distorted line. So even though the reflections were about 320 times weaker they still have influence on the measurement. Newer VNAs have this time windowing option build into the measurement device itself. Allowing measurements to be time windowed without the influences of reflections.

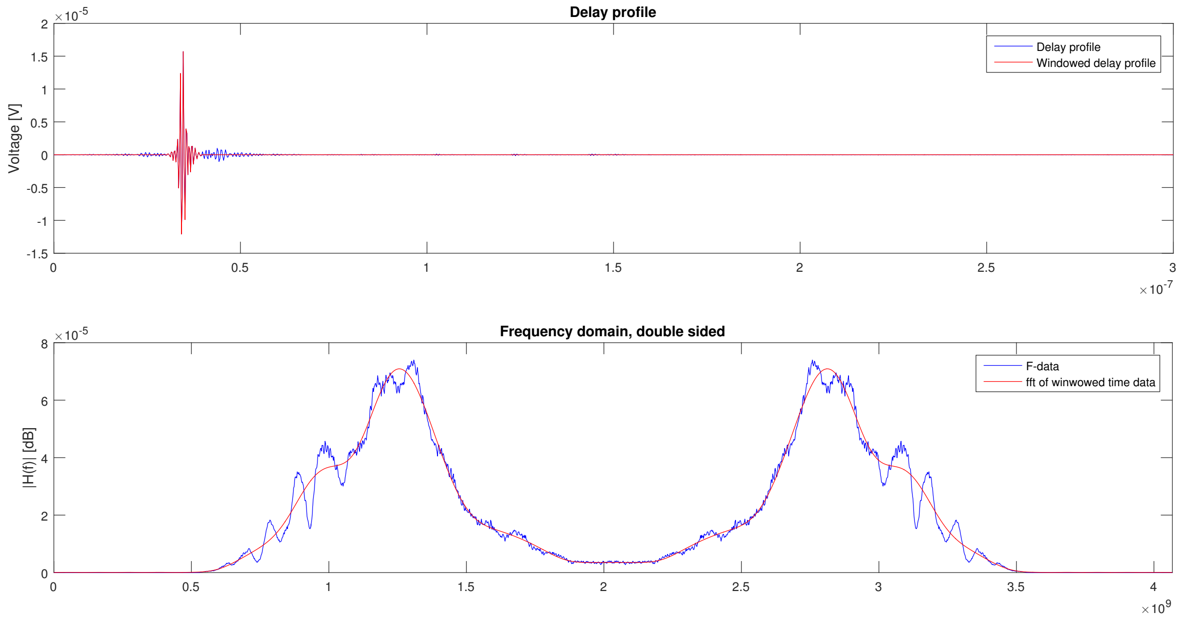

Figure 4.13: Windowed time signal Fourier transformed. The delay profile is zoomed in to show $0 < t < 3.0e-7$

It should however be noted that this calculation is just a crude try to see if there could be something said about the reflections in the chamber. These results should be taken with a grain of salt as for example the time window in Figure 4.13 is taken somewhat arbitrary. Also a rectangular time window was taken. This might also not be the best suited window.

4.4 Conclusion

The objective of this set of experiments was to find the characteristics of the antenna prototype and test if it met the specifications the design had to meet. The research question if the prototype's antennas correspond to ideal dipoles has been answered. The antennas and the ideal dipoles correspond in having only two main lobes and being linearly polarized, two important characteristics. As s said previously, ripples in the antenna pattern cause unpredictability, however these are not present in the radiation pattern of the dipoles. The stronger front lobe compared to the back lobe of the antennas will not cause a issue for the testbed. The Observational Antenna prototype meets all specifications that were set up by Brethouwer, including output impedance and center frequency. The patterns of the three antennas were similar enough to ensure that when multiple antenna prototypes are produced it can be assumed that the patterns will be more or less the same. It is therefore safe to build multiples of the Observational Antenna prototype to be used in the Observational Antenna System of the testbed.

There has also been done some research into the influence of reflections of the anechoic chamber. These influences were present but were not strong enough to lead to different conclusions.

4.5 Recommendations

The next step for the Observational Antenna system is to built multiple antennas from the prototype. The radiation patterns showed that the radiation pattern of each antenna is a little bit pulled back. This might be reduced by changing the antenna PCB material to one with a lower dielectric constant, however the antennas can still be used even though this effect occurs. If multiple antennas were to be constructed it is advised to create an automated measurement system. Not only will this result into better measurements allowing averaging of random errors, but it will also greatly reduce the time it takes to characterize the antennas. Manually measuring the radiation pattern for one single observational antenna system is doable, but for manually measuring five it is not advised.

Chapter 5

Astronomical source simulator

The Astronomical source simulator of the testbed is an source that transmits radio waves that represent the radio waves transmitted by an astronomical source. The purpose of the Astronomical source simulator in the testbed is to have a strong signal the receivers can calibrate on. This strong signal will eventually show up as a very bright spot on the fish-eye measurement image.

Signals transmitted by an astronomical source are mostly wideband noise-like signals with very low or no polarization [4, Ch. 3.3.2]. Creating a source that transmits unpolarized signals is a difficult thing to do. However, the observational antennas in the testbed are linearly polarized and cannot distinguish unpolarized from circular polarized signals. Therefore a transmitting source which transmits circularly polarized waves could be used instead. This greatly reduces the complexity for the Astronomical source simulator. Only one transmitting antenna is needed, the Astronomical source antenna, with a single signal generator, the Astronomical source generator. The polarization recovered eventually be read by combining the signals from multiple antennas.

Using only a single circular polarized source has a limitation on the capabilities of the testbed. This is because the testbed is, just as OLFAR, capable of detecting polarizations of incoming radio waves [15]. The polarization properties of an astronomical source also carry interesting information. Not all astronomical sources are unpolarized, for example a pulsar, a rapidly rotating neutron star, transmits strongly polarized radio waves [5, Ch. 11.6]. If a more realistic source would be used, one that is capable of transmitting with any polarization, the ability of the testbed to detect polarizations could be used as well. One way to accomplish this is to add a second antenna and generator to the Astronomical source simulator that also transmits a circular polarized wave. By altering the direction of rotation and the phase between the two antennas one could generate signals with any form of polarization.

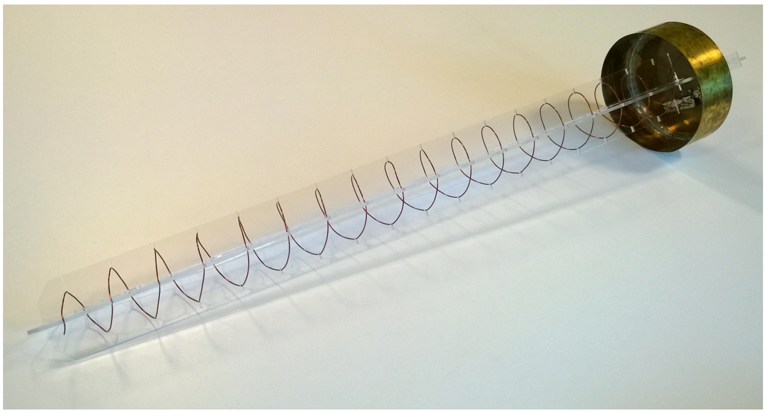

(a) Overview

(b) On stand

Figure 5.1: Astronomical source antenna

M.F. Brethouwer already designed, build and characterized a source antenna to be used as the Astronomical source antenna in the testbed [4, Ch. 4]. The Astronomical source antenna can be seen in Figure 5.1. The source antenna operated properly during the characterisation. For the signal generation Brethouwer used the Agilent E4438C vector signal generator. This generator was more than capable to generate the required signals, however it is also an expensive instrument. Therefore it is not suited for the conditions of in-field testing. Preferably the vector signal generator is replaced with a cheaper alternative. Another remaining task Brethouwer left for future work is measuring the quality of the signal send by the source simulator, as there was no equipment to measure this available during his thesis. This measurement is not preformed during this thesis project as the results of this measurement are only relevant once the testbed is operational.

As part of this thesis project the possibility to use the Nuand bladeRF SDR for the signal generation was explored. This receiver was picked by Brethouwer to be used in the Observational Antenna System and is a relatively cheap alternative. For this research topic the following research question was set up:

Sub-research question:
Can the Nuand bladeRF software defined radio be used for signal generation in the Astronomical source simulator?

The specifications of the Astronomical source simulator given by Brethouwer state that the generator should be able to transmit an 1 MHz bandwidth noise signal at two possible center frequencies of 1271.5 MHz and 1294.1 MHz [4, Ch. 4.1]. From the specifications of the Nuand bladeRF given in Appendix C the operating frequency range of the receiver is 300 to 3800 MHz. As the two center frequencies lie in this operating range this means the bladeRF is capable of transmitting at these frequencies. The specifications also state the instantaneous bandwidth of the device is 28 MHz. Generating a 1 MHz bandwidth noise signal should therefore be no problem for the receiver. So in theory the bladeRF could be used as the Astronomical source generator. One thing that should be kept in mind however is the required transmit power is needed for using the testbed. This is something that can only be determined once the testbed is used in the field as it depends on parameters such as the distance and the presence of RFI sources. If needed the output of the bladeRF could be amplified using an off-the-shelf amplifier.

5.1 Specifications

As was already mentioned, Brethouwer stated the specifications for the Astronomical source simulator [4, Ch. 4.1]. These specifications are listed below:

- Transmit with a center frequency of 1271.5 MHz
- Transmit with a center frequency of 1294.5 MHz
- Generate noise with a bandwidth of 1 MHz
- Generate a circularly polarized output signal

5.2 Method

Recently the software for the bladeRF receivers was updated. This update included improved support for MATLAB and Simulink. These updates will be further discussed in Chapter 7. The new functions for MATLAB were used to program the bladeRF to transmit the 1 MHz bandwidth limited noise. The MATLAB code can be found on the USB stick provided with this thesis.

The measurement is performed in the anechoic chamber using the Astronomical source antenna as the transmitting antenna and the Observational Antenna Prototype as the receiving antenna. The output is received and analysed using a second bladeRF receiver running the MATLAB spectrum analyser script provided by Nuand. The transmitting bladeRF is configured to output maximum power, which is 6 dBm [16].

Using Friis transmission equation one could calculate the gain of the transmitting and receiving antenna pair ($G_t + G_r$) when the received power P_r in dBm is measured

$$P_r = P_t + G_t + G_r - 10log\left(\frac{4\pi r^n}{\lambda^2}\right),$$

where P_t is the transmitted power in dBm, G_t and G_r the antenna gains in dB, R the distance in meters between transmitter and receive, n the path-loss exponent (2 for free-space) and λ the wavelength in meters.

Unfortunately there are two problems using this setup that make it impossible to determine the gain of the antenna pair. The first problem being that the Friis transmission equation only holds when three conditions are met; the distance r between transmitting and receiving antennas is much greater than the wavelength λ, the distance r is much greater than the largest dimension of each antenna and the antennas lie in each others far-field. The first condition is met as the wave length λ of about 0.24 m is small compared to distance r which was about 2.15 m. The second condition however is not met as the biggest dimension D of the Astronomical source antenna is quite big, about 1 m. In the setup the antenna was therefore not placed far enough away as R was not much greater than D. To make matters worse the far-field of the Astronomical source antenna is determined by the Fruanhofer distance [14] equal to

$$d_f = \frac{2D^2}{\lambda}, \tag{5.1}$$

where D is the largest dimension of the antenna and λ the wavelength of the signal.

Using Equation 5.1 with a largest dimension of 1 m results into in a far-field distance of more than 8 m. This distance is not achievable in the anechoic chamber and therefore also the third condition could not be met. A second problem using this setup is that the spectrum analyser script does not show the actual received power by the bladeRF, the scale is only indicative. To get the actual received power one should first calibrate the receiver using a RF power meter, set-up a internal calibration routine using the devices loop back or use a spectrum analyser instead of the bladeRF. However to get as close to the actual application of the testbed the measurement was conducted using a bladeRF as the receiver.

Even though the antennas cannot be separated far enough in the anechoic chamber, the measurement can still show if the bladeRF can transmit the required signals. It is important to know if the cables and transmitting antenna do not distort the signal or decrease its bandwidth, which can still be shown using this setup. Figure 5.2 shows the spectrum of the transmitted noise signal. The signal is generated by filtering a white noise signal, with a filter that has a passband ripple of 1 dB and stop band attenuation of 60 dB.

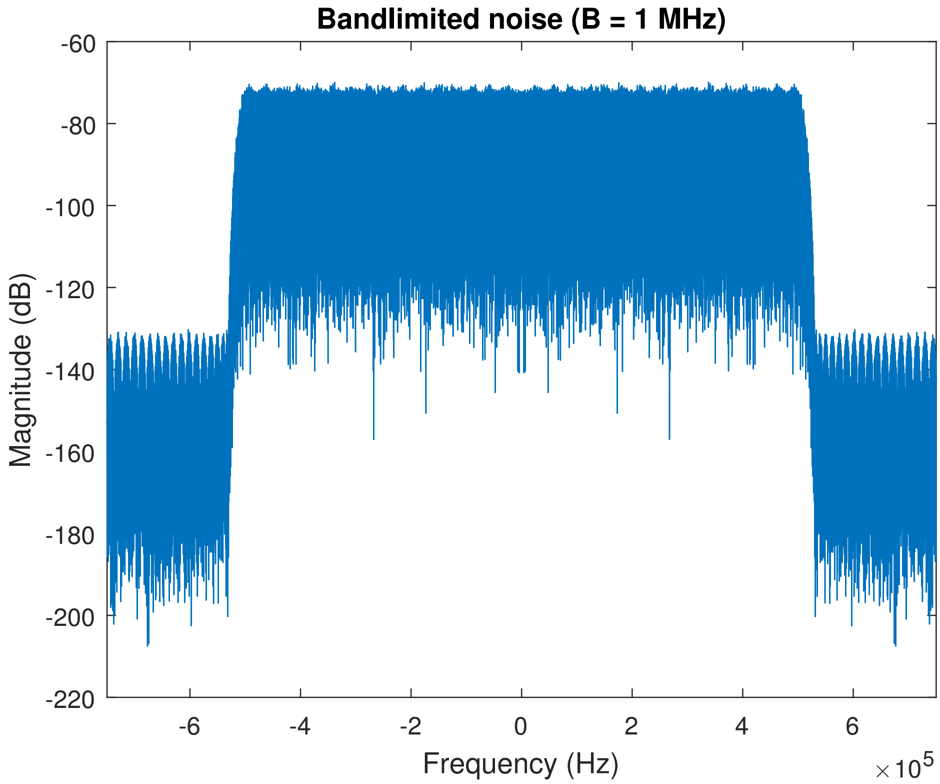

Figure 5.2: Spectrum of noise signal

5.3 Results

Figure 5.3 shows a screen shot of the spectrum analyser script while the noise signal is transmitted in the first band using a center frequency of 1271.5 MHz. The measurement in the second band showed similar results and is therefore omitted. The receiver has three gain control elements, the input low noise amplifier (LNA) and two variable gain amplifiers (VGAs). The gain of the first LNA in was set to its maximum of 6 dB to get the best signal-to-noise ratio (SNR) performance. The gains of the first and second VGA are kept at their minimum of 5 dB and 0 dB respectively.

The spectrum of Figure 5.3 shows that the noise signal is received with the same bandwidth of 1 MHz as is transmitted by the transmitting bladeRF without distortion. The spike in the center of the spectrum is caused by an common issue in the direct-conversion receiver topology the bladeRF uses [17]. The direct-conversion receiver, also known as homodyne receiver, down-mixes the pass-band signal with a frequency equal to the carrier frequency, converting the signals directly to base-band. The spike is caused by leakage of the local oscillator generating mixing frequency in the receiver path which manifests itself as a DC offset after down-mixing. The bladeRF has some calibration routines for compensating the DC offset created by the local oscillator that could be used to reduce the magnitude of this spike.

The figure also shows that the noise floor has two levels a 27.5 dB lower than the incoming signal. The lowest existing around -100 dB, while a higher one exists around -95 dB. The reason that there are two levels in the noise floor is because of the bandpass input filter of the receiver. This one is set to the lowest setting of 1.5 GHz, which corresponds to the higher level in the figure.

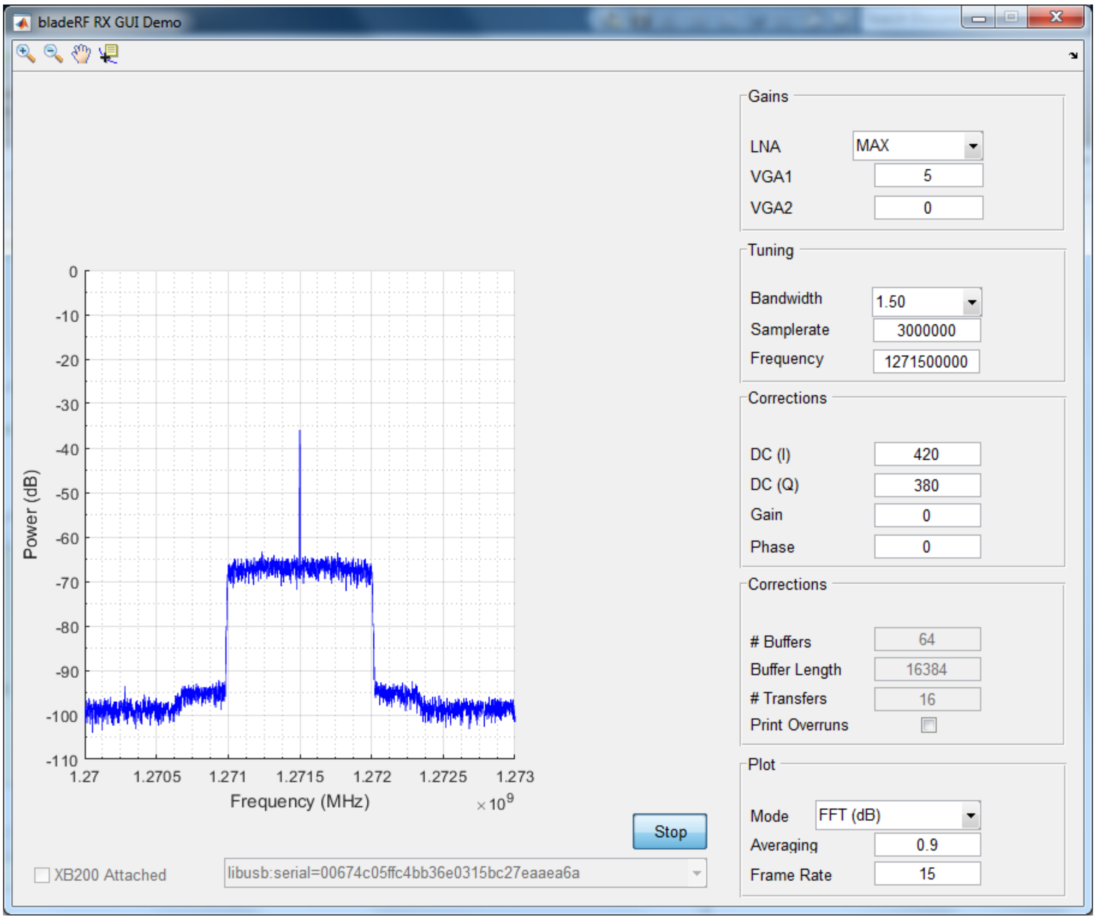

Figure 5.3: Spectrum of received signal using lowest gain settings; LNA1 gain of 6 dB, RXVGA1 gain of 5 dB and RXVGA2 gain of 0 dB

One should keep in mind though that the noise floor in this setup is very low because the experiment was performed in the anechoic chamber which works as a Faraday cage as well, blocking most outside RFI. When the testbed is used in field the noise floor will be considerably higher. To compensate for this higher noise floor the gain of the receivers could be adjusted.

5.4 Conclusion and recommendations

The measurements showed that the Nuand bladeRF software defined radio can indeed be used as the signal generator for the Astronomical source simulator. When the testbed is used in the field it is useful to know the antenna gains of the Astronomical source antenna and the Observational Antenna. If the source antenna will be located at a distance of 50 m from the Observational Antenna System the path loss can be calculated by

$$L = 10log\left(\frac{4\pi r^n}{\lambda^2}\right),$$

where r is the distance, n the path-loss component and λ the wavelength.

When the testbed is used in field the path-loss component is around 3.5 [18]. Resulting in a path loss of more than 80 dB. As the bladeRF can only transmit with a power of 6 dBm it is likely that an amplifier should be added to get a reasonable SNR. The required transmit power can be calculated using Friis transmission equation once the antenna gains of the Astronomical source antenna and the Observational Antenna are known. Measuring the gains of the antennas is left for future work once the testbed is near completion.

To increase the functionally of the testbed a second Astronomical source antenna and generator could be added. This way any arbitrary polarized signal could be send, including un-polarized signals.

Chapter 6

Receivers

The receivers of the testbed will convert the received radio signals of the observational antenna system to digital data. The acquired data can then be fed to the calibration and RFI mitigation algorithms for OLFAR. Brethouwer already picked a suitable receiver in his thesis. His choice fell on the Nuand BladeRF SDR because it has an Altera Cyclon IV field programmable gate array (FPGA) on board which can be programmed to fulfil various tasks. A picture of the BladeRF is shown in Figure 6.1. One of these tasks is clock synchronisation system as which will be present in OLFAR. The specifications of this SDR can be found in appendix C.

Brethouwer states in his thesis report that the loop filter used in the phase locked loop (PLL) for clock synchronisation was very primitive and should be improved before the testbed could take actual measurements [4, Ch. 6]. His implementation of the loop filter lacked a proper integrator to reduce clock jitter created by the phase detector of the PLL. The PLL also coped with an electro magnetic compatibilty (EMC) problem causing the measurement to fail half of the time. To find out how the PLL should be modified the following research question was set up:

Sub-research question:
How should the PLL used in the receivers of the testbed be improved to have reliable and accurate clock synchronisation?

In the next sections the implementation of the clock synchronisation in the testbed is explained and related to the clock synchronisation of OLFAR. Next, the issues with the current implementation of the loop filter are discussed. Some research in finding an improvement for the loop filter is done and a few proposals are given. Because there was not enough available time the improvements could not yet be implemented. Implementing these is therefore left for further work on the testbed.

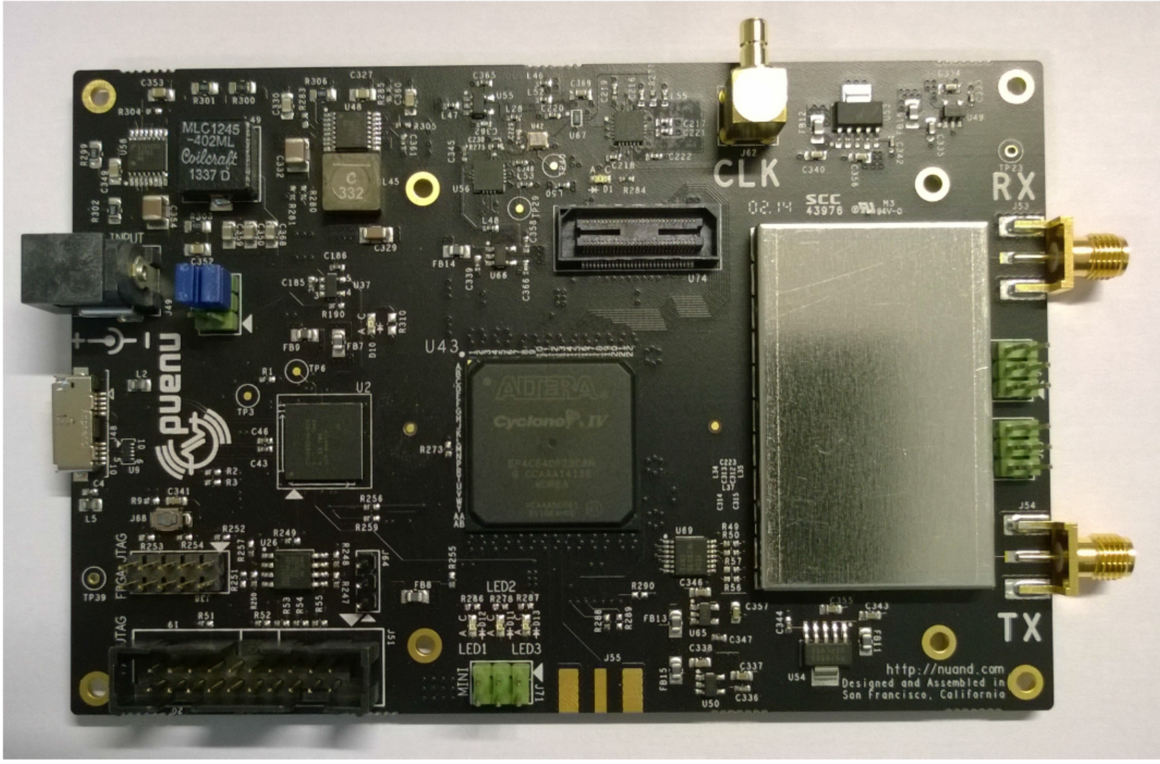

Figure 6.1: The Nuand BladeRF software defined radio

6.1 Requirements

Brethouwer set up a list of requirements for the receivers which can be found below:

- Frequency range from 1271 to 1295 MHz
- Bandwidth greater than 1 MHz
- 50 Ω input impedance
- Stable oscillator
- High sample rate
- Capable of real-time data processing
- Capable of clock sharing
- Capable of clock synchronization

Of these requirements the first eight were inherently met by choosing the BladeRF as the receiver to be used in the testbed. The last one can be met by modifying the firmware of the receiver [4, Ch. 6].

6.2 Clock synchronisation

To perform the interferometry the clocks of the receivers in OLFAR have to be synchronised. Each satellite has three receivers, one for each antenna. As these receivers are inside the same satellite they can share their clock before and during the measurement. The synchronisation between satellites is done before the measurement starts. This is because the communication between satellites required for synchronisation during a measurement would disturb the measurement. During the measurement the receivers stop synchronising and clocks of each satellite will start running free. This will cause the clocks to drift with respect to each other.

The firmware of the receivers used in the testbed has been modified to mimic the clock distribution in OLFAR. Figure 6.2 shows the clock distribution of the receivers for a complete testbed with five satellite mock-ups and 15 receivers. The receivers are used in a multiple input multiple output (MIMO) setup. The testbed uses three configurations for the receivers of the testbed: A MIMO slave, a MIMO master with PLL and a global/MIMO master. The three configurations will be briefly discussed in the following section. A more detailed explanation of the configurations can be found in Brethouwers thesis.

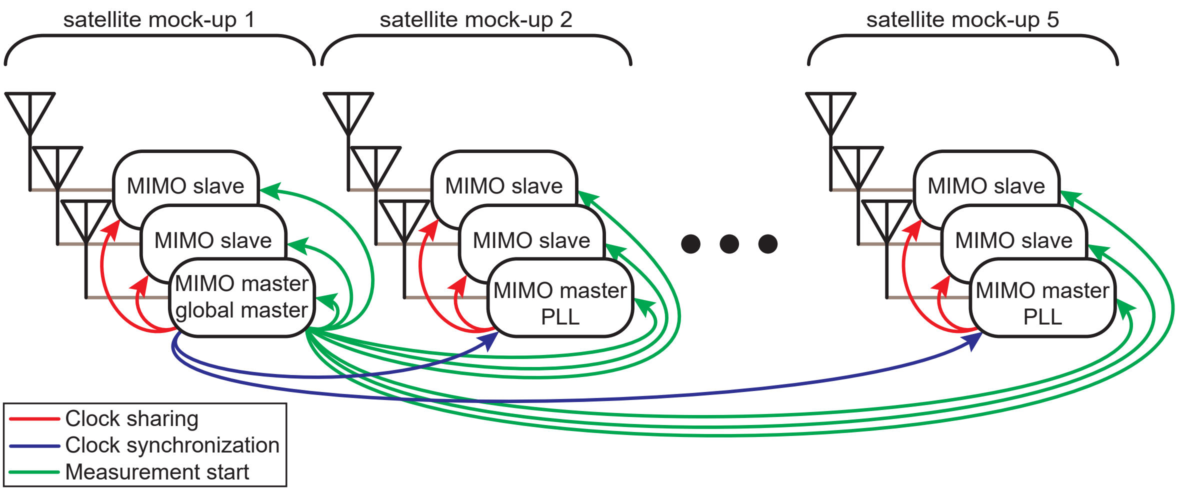

Figure 6.2: The clock distribution of the testbed [4]

Global/MIMO master

The testbed has one receiver that is configured to function as the global master of the testbed. The global MIMO master has two additional functions compared to the other MIMO masters. The first one is that it provides the global clock signal all the other MIMO masters can synchronise with. The second function is the generation of a “measurement start” signal. This signal is used to tell the receivers in the testbed to start recording the antenna signals. Just as the other MIMO masters the clock of this receiver is shared with the receivers in the same satellite mock-up.

MIMO master with PLL

The other four masters in the testbed are configured as MIMO masters which share their clocks with the MIMO slaves inside the same satellite mock-up. Before the measurement the MIMO masters synchronise their clocks with the global/MIMO master using a PLL implemented on the FPGA. Details on the PLL will be discussed in 6.4. After the “measurement start” signal is received by the MIMO master it will stop synchronising with the global/MIMO master and the clock will continue in free running mode.

MIMO slave

The other receivers are configured as MIMO slaves. These slaves use the (external) clock provided by their MIMO master. After receiving the “measurement start” signal they will also start the measurement.

6.3 Measurement cycle

The measurement cycle of the testbed consists of four stages. The initialization stage, the synchronisation stage, the measurement stage and the processing stage. The cycle is controlled by a computer running MATLAB that communicates to the receivers by their USB connections.

During the initialization stage the receivers are programmed and configured with the required settings like operating frequency, bandwidth, sample-rate and gain. After the initialization, the global master is set to a five second countdown before it sends out the “measurement start” signal. After the “measurement start” signal is send all the receivers go into the synchronisation stage. During this 20 second period the MIMO masters synchronise their clocks to the global/MIMO master. To compensate for the lack of an integrator in the loop filters of the MIMO master’s PLL the output of the loop filter is averaged during this 20 second period. After this synchronisation period the MIMO masters take their last averaged value and stop synchronisation with the global/MIMO master. The testbed now enters the measurement stage and the received data is streamed to the computer. The receivers sample the signals for the set sample time after which they stop receiving. In the final stage, the processing stage, the data is processed using MATLAB on the controlling computer.

6.4 Phase Locked Loop implementation

Figure 6.3 shows how the internal clock of the BladeRF receiver is generated. The clock generation of consists out of four elements. A voltage controlled temperature compensated crystal oscillator (VCTCXO) provides a 38.4 MHz clock signal for the Si5338 clock synthesizer chip. This chip generates the two transmit and receive sample frequencies as well as a carrier frequency for the LMS transceiver chip. It also generates the clock signal and a transmit clock for the FPGA. The VCTCXO is connected to a digital to analog converter (DAC) which can tune the oscillator. The FPGA gives a constant value to the DAC that gives the VCTCXO the correct frequency. This constant value is determined during factory calibration.

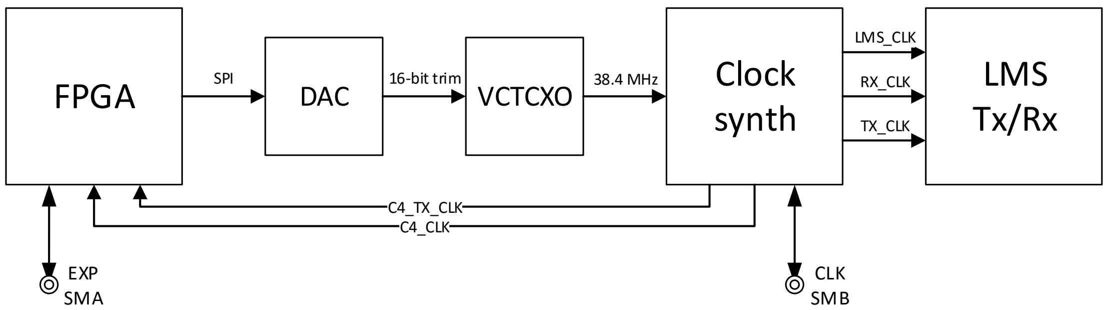

Figure 6.3: The internal clock distribution of the BladeRF receiver. The USB3 controller is omitted from the drawing as it is not of interest.

The clock synthesiser chip also has an external SMB connector on which either the internal clock can be outputted or an external clock can be inserted. In the testbed all the MIMO masters output their internal clock to this connector. On the MIMO slaves the connector functions as an input to take the clock from the MIMO masters as an external clock. Because the MIMO slaves do not run on their own clock the VCTCXO and the trim DAC of these receivers are not used and are disabled.

For synchronising the receivers in the testbed a digital PLL is used. A block diagram of a digital PLL is shown in Figure 6.4. A digital PLL consists of 4 elements, the phase detector (PD), the digital loop filter, the digital controlled oscillator (DCO) and a optional divide by N block in the feedback loop. The divide by N block scales the output frequency of the PLL to be N times the reference frequency.

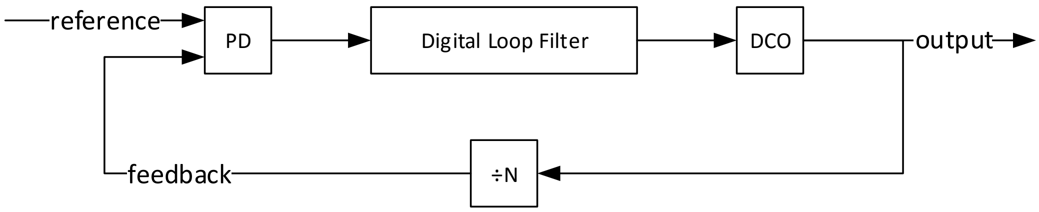

Figure 6.4: Digital PLL with divide by N feedback loop

In the MIMO masters with PLL the operation of the trim DAC and the VCTCXO is altered to mimic the way the receivers in OLFAR are synchronised. Figure 6.5 shows the modified clock generation inside these receivers. The DAC and VCTCXO together form the DCO of the digital PLL instead of just being used for factory calibration. A PD and loop filter are implemented on the FPGA to complete the PLL. The reference clock for the PLL is provided from the global master through the general purpose expansion SMA connector on the bottom side of the board. The feedback signal for the PLL is the clock signal provided by the clock synthesizer chip.

The digital PD in Brethouwer's design is implemented as an Alexander phase detector. This PD is of a non-linear 'bang-bang' type, meaning it gives only two output states indicating if the clock is leading or lagging compared to the reference clock. In literature PLLs using this PD are therefore sometimes called lead-lag PLLs [19]. This type of PD is normally used in clock-data recovery circuits because it automatically retimes the incoming data [20]. As the synchronising in the testbed does not concern a clock-data recovery circuit this advantage is inapplicable in this case.

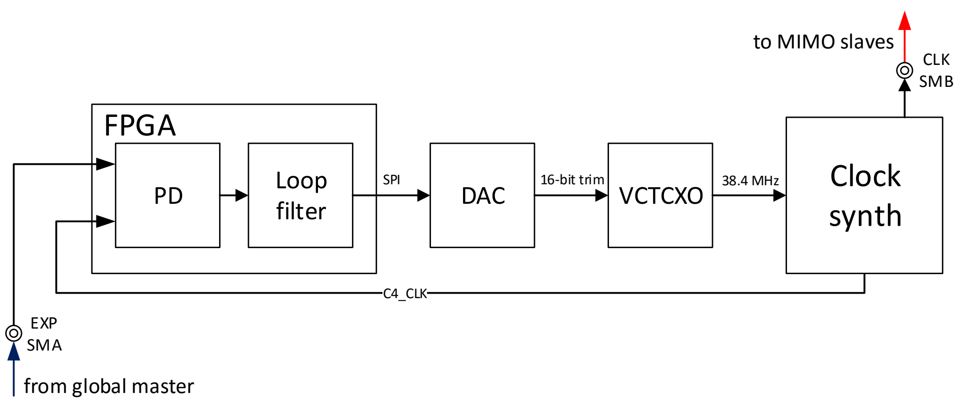

Figure 6.5: The PLL implementation inside the MIMO master with PLL receivers.

However, the non-linear behaviour gives this PD a very high gain for small difference in phase, which reduces the steady-state error. A disadvantage however, is the high output jitter the PD produces. In an analogue PLL this PD is therefore almost always followed by a first-or second-order low-pass filter to integrate the output of PD and reduce clock jitter. Brethouwer did however not have the time during his thesis project to design a proper loop filter. His implementation for the loop filter consisted only of a proportional gain and a averaging period. Because of the non-linear behaviour of the Alexander phase detector the loop filter should include an integrating element to ensure stability and reduce output clock jitter.

6.4.1 Issue with the current implementation

Besides the PLL implementation in the MIMO masters with PLL lacking an integrating element in the loop filter there was also an EMC problem. Brethouwer states this problem in one of his notes added to his thesis. The problem manifested inside the MIMO master with PLL receiver and occurs after the measurement start signal is sent. The result was that half of the time PLL started to behave strangely after the "measurement start" signal was received. Brethouwer states that the problem either has to do with the data transfer to USB or the presence of ground loops and that improving the loop filter should fix this problem.

Upon further examining this problem it was noted that the FX3 USB3 controller chip uses the same output from the VCTCXO as the clock synthesizer chip does as shown in the schematics of the BladeRF [21, Sheet 12]. When the measurement start signal is received the loop filter starts its averaging period. After this period the DAC is set to the averaged value causing the frequency of the VCTCXO to jump to a different frequency. As the USB3 controller chip uses the output of the VCTCXO this jump might cause it to glitch and lose contact with the controlling computer. This is the disadvantage of using averaging instead of a proper integrator. If this is the case then the issue Brethouwer experienced might not be due to EMC problems or ground loops, but just due to the poor loop filter.

Either way the loop filter has to be improved for the testbed to function properly. The next section will discuss how this improvement can be made.

6.5 Improvements for the loop filter

The loop filter of a PLL determines most of the PLL's performance. These include the bandwidth, settling time, steady-state error and most importantly, stability. Designing loop filters for PLLs can take quite a lot of time. Luckily there are a few known standard loop filter configurations that might be used to improve the PLL of the receivers that perform adequately. Some research has been done on the improvement of the loop filter in the receivers. The next sections discuss a few possibilities.

6.5.1 N counter

One of the simplest loop filters that can be implemented is the N counter [22], [23]. The N counter is simply a n-bit counter block that is controlled by the output of the PD. The N counter is particularly useful when a non-linear lead/lag PD is used, as it can operate on simple lead/lag input pulses of arbitrary length. Figure 6.6 shows the block diagram of the N counter.

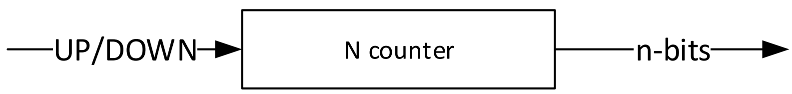

Figure 6.6: The N counter loop filter

When the DCO in the PLL operates on the center frequency the counter has a specific nominal value N (normally half the maximum value of the counter). The up pulses add to, and the down pulses subtract from the counter. The output of the counter can be seen as an average of the PD pulses. This is described in the discrete-time z-domain as [22]

$$n_{out}(z) = (1 + z^{-1} + z^{-2} + z^{-3} + ...)\theta_d(z), \tag{6.1}$$

where $n_{out}(z)$ is the counter value and $\theta_d(z)$ are the output pulses of the PD, either $+1$ or -1. Noting that equation (6.1) is a geometric series the transfer function of the n-counter can be written as

$$\frac{n_{out}(z)}{\theta_d(z)} = \frac{1}{1 - z^{-1}} = \frac{z}{z - 1}, \tag{6.2}$$

which is an integrator with an added zero at $z = 0$ [22].

The angular frequency of the voltage controlled oscillator (VCO) on the receivers is given by [23, Ch. 2] as

$$\omega_{vco} = \omega_0 + \Delta\omega(t) = \omega_0 + K_{vco} u_f(t),$$

where K_{vco} is the VCO gain in $rad \cdot s^{-1} \cdot V^{-1}$ and $u_f(t)$ the analogue control signal applied on the VCO. In case of the receivers this analogue control signal is provided by the trim DAC.

The phase transfer for the VCO operating at the center frequency ω_o is simply the time integral of the angular frequency change $\Delta\omega(t)$,

$$\theta_{vco}(t) = \int \Delta\omega(t) dt = K_{vco} \cdot \int u_f(t) dt.$$

In the s-domain, the time integration is just a division by s

$$\theta_{vco}(s) = K_{vco} \frac{u_f(s)}{s},$$

resulting in the transfer function

$$\frac{\theta_{vco}(s)}{u_f(s)} = \frac{K_{vco}}{s}. \tag{6.3}$$

Using the bilinear transform the discrete time domain transfer is:

$$\frac{\theta_{vco}(z)}{u_f(z)} = K_{vco} \cdot \frac{T(z+1)}{2(z-1)} \tag{6.4}$$

where T is the discrete time step. In the case of the BladeRF that would be the update period of the trim DAC which is $(200kHz)^{-1} = 1 \cdot 10^{-5}s$ [4].

Combining Equation (6.2) with Equation (6.4), using the counter output as the VCO control, $n_{out}(z) = u_f(z)$ gives the open loop transfer of the PLL

$$\frac{\theta_{vco}(z)}{\theta_d(z)} = \frac{K_{vco}T}{2} \frac{z(z+1)}{(z-1)^2},$$

which is a second order transfer with poles inside the unit circle and is therefore stable.

A simple counter would therefore suffice as a loop filter for the receivers. If the counter were to saturate to either the maximum value or minimum value, the gain of the loop filter would decrease, but it would not destabilize the PLL [22]. The trim DAC on-board of the receiver is 16-bit DAC, therefore the obvious size of the N counter would also be 16 bits. Additional bits would be decimated, and would offer no advantage.

6.5.2 Linear phase detector and the K counter

The PLL of the MIMO masters will operate closely to the center frequency of 38.4 MHz as all the internal oscillators of the receivers run on this frequency. The advantage of the high gain of a non-linear PD then becomes marginal. Therefore the choice could be made to swap the Alexander phase detector with a linear PD like an XOR or JK-flip flop detector. These PDs give square wave signal with a duty cycle that is linearly proportional to the phase difference. The advantage of using a linear PLL is that linear design techniques can be used to the design the PLL.

In a linear all digitial phase locked loop (ADPLL) a K counter can be used as a loop filter [23]. The K counter is similar to the N counter, however it uses two counters, the up counter and the down counter. Figure 6.7 shows the block diagram of the K counter.

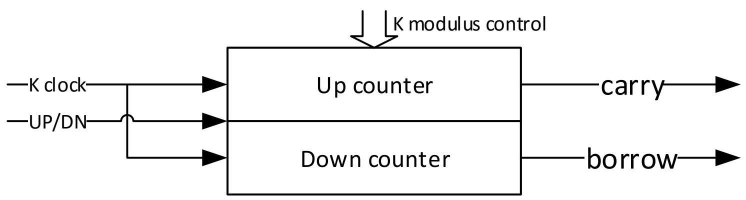

Figure 6.7: The K counter loop filter

The counters operate on an clock signal, the K clock, which is by definition M times the center frequency of the PLL. Every clock cycle of the K clock one of the two counters counts while the other stays frozen. The $DOWN/\overline{UP}$ control line determines which of the two counters is counting. This signal is the duty cycle coming from the linear phase detector. The K counter has two outputs, the carry and the borrow output. If the contents of the up counter exceed $K/2$ the carry output is high. Similarly the borrow output is high when the contents of the down counter exceed $K/2$. Both counters reset to 0 if one of the counters exceeds the value $K - 1$. An addition control signal called K modulus controls the size of the counters.

The output carry and borrow pulses directly control the DCO. When a carry pulse is send the DCO increases in frequency while a send borrow pulse will decrease the DCO in frequency.

Section 4.3 of the book Phase Locked Loops by Roland E. Best [23] discusses the specifications of the K counter loop filter. For this loop filter the frequency-domain phase transfer function is

$$\frac{\theta(s)}{\Delta_K(s)} = \frac{M\omega_0}{Ks},$$

where $\Delta_K(s)$ is the Laplace transform of the PD's duty cycle signal and ω_0 is the center frequency of the PLL.

For this loop filter the frequency range in which it holds a lock is equal to:

$$\Delta f_H = f_0 \frac{M}{2KN} \; for \; N > \frac{2M}{K}$$
$$\Delta f_H = \frac{f_0}{3} \; for \; N < \frac{2M}{K},$$

where f_0 is the center frequency of the PLL.

The loop filter is a first-order system and has a bandwidth of

$$f_{bw} = \frac{K_d \pi M f_0}{KN},$$

where K_d is the gain of the PD used in the loop.

6.5.3 Advanced digital loop filter design

If above mentioned loop filter solutions prove to be inadequate more advanced loop filters could be designed. The paper *A Design Procedure for All-Digital Phase-Locked Loops Based on a Charge-Pump Phase-Locked-Loop Analogy* [24] describes for example how an proportional-integrating loop filter can be designed from an analogue prototype. The digital loop filter is of the first order and has the transfer function equal to

$$\frac{\theta_{out}(z)}{\theta_{in}(z)} = K_p + K_i \frac{1}{1 - z^{-1}},$$

where K_p is the proportional gain and K_i the integrating gain. The paper gives a method of designing the PLL by specifications as phase margin and operating bandwidth.

If even more freedom is needed in the loop filter, digital Finite Inpulse Response (FIR) or Infinite Impulse Response (IIR) filters could be designed. These work better with a Time to Digital Converter (TDC) added after the PD. A TDC gives a digital output number for the phase difference given by the PD. With the transfer function of the DCO is given by Equation 6.3, the whole PLL can be modelled in Matlab after which a system control design strategy can applied. The only unknown that remains is the VCO gain K_{vco}. This could however be easily measured by controlling the trim DAC output voltage and measuring the output frequency via the clock SMB connector on the receiver.

6.6 Conclusion

In this chapter the current state of the receiver system for the testbed was discussed. The chapter provides a detailed description on how the clock synchronisation is implemented so the person who continues the work on the testbed would not have to take the extra effort in researching. The current issues with the synchronisation are highlighted and a few suggestions for improving the loop filter in the PLL of the receivers are given.

During this thesis project there was not enough time to implement an improvement for the loop filter as the focus was put on the completion and characterisation of the Observational Antenna prototype. The next step for implementing the receivers of the testbed is to try the suggested loop filters in the order in which they are discussed, and see if this solves the issues mentioned in Section 6.4.1.

Chapter 7

Software

The software of the testbed controls all the features of the testbed. It communicates with the receivers, configures the receivers, controls the measurement and handles the data processing. For controlling the testbed, the open source software of Nuand, the manufacturer of the SDRs, has been modified to incorporate new functionality by Brethouwer. This open source software consists of a C library containing all the functions to control the bladeRF and a command line interface executable. Brethouwer implemented scripts in MATLAB that uses this command line interface so the whole testbed can be controlled using MATLAB. Using MATLAB makes it possible to integrate the algorithms for calibration and RFI mitigation directly into the software for the testbed.

Brethouwer created a complete package for controlling the testbed. All necessary features are implemented and are well documented in his thesis and the source code has been provided on the DVD. The software is in a state where the algorithms for OLFAR could directly be implemented. Because the software is in a state where it is ready to be used, there was not anything modified to it during this thesis project. However, as part of the preparatory work of this thesis project some time was spent to get to know the software so it could be altered if necessary. During this process some changes and updates to the software and firmware by Nuand were found, that were published after Brethouwer finished his thesis, that may be used to improve the testbed. In the next sections the most important changes are presented and their influence for the testbed is discussed.

7.1 Updates to software

Nuand is constantly updating the software and firmware for the bladeRF by adding new features and solving existing problems. After Brethouwer finished his thesis project new features were added like the possibility to quickly switch frequencies, new DC calibration routines, oscillator taming for increased stability, a redesigned NIOS softcore and redesigned MATLAB & Simulink support. The latter two have some consequences for the testbed and will be discussed in the next two sections.

7.1.1 Redesigned NIOS core

The software of the testbed has to be upgraded to the newer versions of Nuand to take advantage of the new features like the improved DC calibration routines. If the choice is made to upgrade, some alterations have to be made in the new functionality added by Brethouwer. The main reason for this is the redesigned NIOS II core. The NIOS II core is a soft-core processor running on the FPGA of the bladeRF. It runs C code and communicates with other parts of the FPGA via IP cores.

The NIOS II core handles all communication from and to the bladeRF. Figure 7.1 shows where it is implemented in the receiver. The main change after the redesign is the method of sending packets back and forth between the bladeRF and the controlling computer. The redesign allows for more intuitive packet handling and easier addition of new packets for custom commands or new functionality.

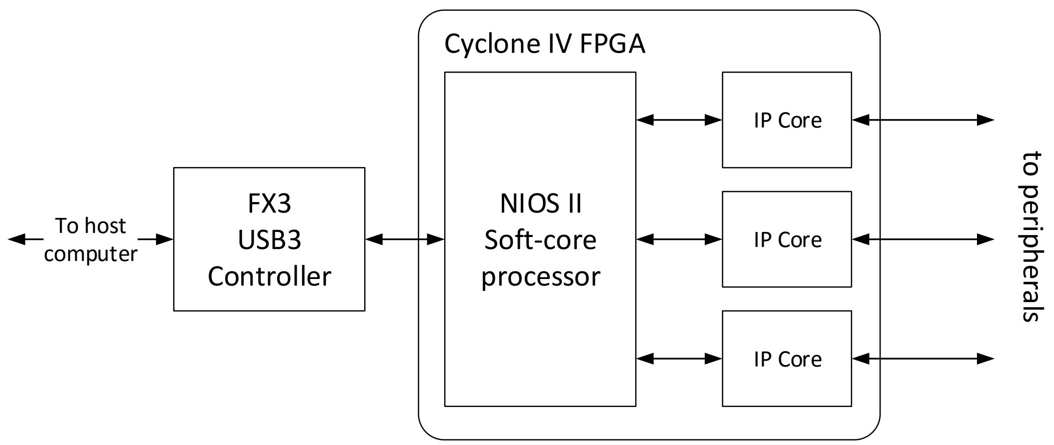

Figure 7.1: The NIOS II soft-core processor of the bladeRF

A manual has been added to the USB drive included with this thesis, explaining how new functionality should be added to the testbed. An example has been created for blinking one of the 8 LEDS on the expansion board of bladeRF. The example lets the user select the LED that should blink with a command that has been added to the command line interface executable. The source code for this example can also be found on the USB drive. It is recommended that the rest of the testbed software is also updated to the newest versions as it allows for easier addition of functionality.

7.1.2 Redesigned MATLAB & Simulink support

Another update to the bladeRF software is the improved support for MATLAB and Simulink. The bladeRF can now be controlled in full duplex from either a MATLAB script or a Simulink model. The underlying code directly uses the libbladeRF library that is also used by the command line interface. The script for using the bladeRF as the source generator for the Astronomical source simulator uses this new MATLAB functionality. The MATLAB code can be found on the USB drive. Also, a demo was created using Simulink that transmits the sound of a pulsar using frequency modulation from the Astronomical source simulator to the Observational antenna prototype. Figure 7.2 shows the used Simulink model.

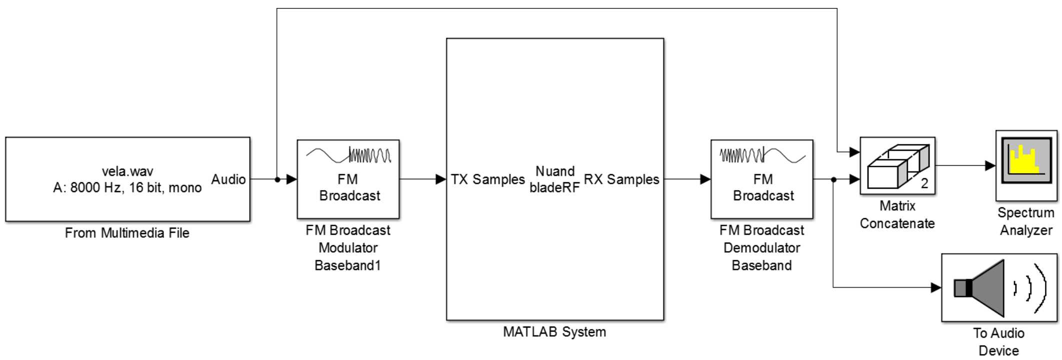

Figure 7.2: Simulink model to transmit and receive a FM modulated signal

The current MATLAB code for the testbed controls the receivers by opening the command line interface window using the 'system' command of MATLAB. This method requires a lot of excess code to create the right command string and parse the resulting text output from the console window. Therefore the choice could be made to directly access the libbladeRF library as is done with the redesigned MATLAB support. The MATLAB files provided by Nuand should give enough information on how the C library can directly be accessed in MATLAB scripts.

7.2 Improved receiver synchronisation

Important for the testbed is that the start of the measured signals is synchronised across the receivers of the testbed. If the measurement is not synchronised this would result into unforeseen time delays causing incorrect images after correlation. Chapter 2 showed that unforeseen delays are detrimental for creating the images.

To synchronise the start of a measurement between the receivers of the testbed, Brethouwer implemented. His implementation ensured that the data received by the receiver chip is marked as invalid blocking the data stream to the computer until the 'measurement start' signal is received. Brethouwers implementation does however not align the received samples across the receivers, because the receive buffers in the FPGA might already contain some samples. This would mean that after the 'measurement start' signal is sent, the location of the first sample containing measured data in the data stream of one receiver does not necessarily match the location of the first sample containing measured data in the data stream of another receiver. They might be misaligned by a few samples. To perform interferometry the samples then have to be realigned after everything is streamed to the computer. This sample offset would cause wrong results as it would be similar to adding a time delay to the signal of one of the receivers. However, receiver delays are one of the parameters that could be calibrated using the developed algorithms for OLFAR. An interesting feature for the testbed therefore would be to have a controllable receiver delay. This controllability is only possible when it can be assured that the initial samples are synchronised.

Another user of the bladeRF by the screen name of 'polygon' has been developing code for synchronised transmitting and receiving with a MIMO set-up of bladeRFs. He solves the problem of aligning samples by resetting the sample counters in the FPGA and disabling the analog to digital converters (ADCs) of the receiver chip until the synchronisation signal is received. Nuand has showed interest in this feature and has already pulled the code into a separate branch called 'dev-synctrx' into the official repository, but has not yet officially released it. The USB drive contains a file with all related discussions on this topic.

Polygon has provided a demo to verify the synchronisation. This demo has two bladeRFs in a MIMO setup, similarly to the setup in the testbed. The bladeRFs all share a clock signal provided by one of the bladeRFs. Also a 'trigger' signal is shared via the expansion header, similar to the 'measurement start' signal in the testbed. His demo uses Python to generate two uncorrelated noise signals, lets each bladeRF transmit one of these signals while simultaneously receiving both signals. The bladeRFs start transmitting and receiving in synchronisation after a command on the computer is send to the first bladeRF. He then proves that the signals are transmitted and received in full synchronisation by correlating each received signal with both transmitted signals, including the one send by itself. The result is a correlation plot which shows the four correlations peak at exact the same sample. The whole demonstration is described in a Python notebook of which the link can also be found on the USB drive. His demonstration has been verified with two of the receivers of the testbed. This showed similar results with correlations peaking at the same sample location.

The improved synchronisation is very interesting for the testbed. As it would solve the problem of misaligned samples in the data streams of the receivers and would give the possibility for controlled receiver delays. The demo shows the synchronisation working in a similar setup to that of the testbed with synchronised samples, meaning that it should be relatively easy to implement it in the testbed.

7.3 Conclusion

Brethouwer provided a full software package to control the testbed. One of the tasks of this follow-up project was to familiarize with his work so it could be extended if needed. A few improvements such as redesigned command handling, MATLAB control, and measurement start synchronisation were presented that could be added to the software. Because the current software already provides a complete package to control the testbed, it was decided to wait with implementing these improvements until the testbed is in a more complete state. When the testbed is a more completed state all the code can be updated at once to newer versions of the software. This would to take the fullest advantage of the ongoing development of the bladeRF software by Nuand and its users without having to perform updates multiple times during the development process of the testbed.

Chapter 8

Physical Construction

The final component of the testbed concerns the physical construction. The physical construction holds the Observational antenna systems in place to provide stability during the measurements. It should ensure that accurate measurements can be taken, while keeping the testbed portable, easy to set up and use. Finally the physical construction should allow for repeatable measurements to be taken. If a measurement would be conduct twice with the same parameters the result should be the same.

In addition to providing stability and accuracy of the Observational antenna systems, the physical construction should also make sure that the Observational antenna systems are reconfigurable. This is because in OLFAR, the swarm of the satellites does not have a specific structure. The satellites will be moving slowly with respect to each other, however during the measurement they may be considered stationary. Because of the movement of the satellites, the physical construction of the testbed should allow for multiple configurations of the satellite mock-ups. The mock-ups may be moved between the measurements, but should be stationary during a measurement. Relocating the satellites might be done automatically, however this is not required.

Brethouwer created one concept design for the physical construction of the testbed. Durint the work on this thesis, his design concept was initially deliberately not consulted, in the hope of obtaining some fresh independent ideas for this part of the testbed. At the end of this thesis project, Brethouwers design was consulted to compare it with the new ideas and insights gained during this thesis. Brethouwer's design will be reviewed at the end of this chapter. There was not enough time for finalizing the design and building the physical construction during this thesis. However, there were some insights gained that could be used in the final version of the design for the physical construction.

8.1 Specifications

As was already mentioned in Chapter 2 the physical stability of the testbed is essential to perform accurate interferometry. Brethouwer already set up a few specifications for the physical construction of the testbed to conform these stability requirements [4, Ch. 8]:

- Baseline determination accuracy of $\lambda/10$
- Baseline stability smaller than $\lambda/10$ during the measurement
- Antenna orientation accuracy of $1°$
- Antenna spinning rate smaller than $1°/s$

8.2 Design considerations

During this thesis some new insights and ideas were gained that could be used for the final design of the physical construction. These ideas are presented in the following subsections.

8.2.1 Satellite constellations and movement

As was mentioned previously, the physical construction should allow multiple configurations of the five satellite mock-ups to simulate the movement of the satellites in OLFAR. As the satellites of OLFAR are in space, they can have arbitrary location and orientation, having complete freedom in all six-degrees: X, Y, Z, pitch, yaw and roll. This level of flexibility is however not necessary for the testbed because even with limitations still a lot of possible constellations than you can measure can be created. Not everything has to be variable to still have an interesting set of configurations and gain insight full results. Besides that, this level of flexibility is most likely also not feasible to achieve. Hence the boundary conditions for the flexibility will be discussed in the following sections

Height flexibility (Z-axis)

The characterization of the Observational antenna prototype clearly showed the importance of the ferrites on the feed lines to the antennas. If the satellite mock-ups were to be repositioned in height, or Z location, ensuring that there are ferrites on the length of the feed lines would be difficult and would most likely result in a complex construction. An alternative would be to let each satellite mock-up have an antenna pole of different length. This allows for some difference in height between the mock-ups. The height of the poles should be not too short as then the antennas would get too close to the feed lines or the ground. Suitable heights would be between 0.5 m and 1.75 m.

Positioning (X-axis, Y-axis)

The suitable options for repositioning are moving the mock-ups in the X and Y direction. To allow for easier placement the antenna poles could be placed in a set of predetermined possible positions with known locations. This would reduce the time between measurements as it avoided having to measure the distances between each mock-ups after reconfiguration.

Orientation (Pitch, Roll, Yaw)

Adjusting the pitch or roll would be require a tilting set-up close to the antenna PCBs. This would disturb the feed lines and therefore the performance of the antenna. Also achieving precision is difficult using such a setup and is therefore not an option to increase the level of flexibility of positioning the mock-ups. The mock-ups could however be rotated by rotating the antenna pole, as was done during the characterization in Section 4.3.2.

8.2.2 Automated movement

To reduce the time it takes to use the testbed, an option is to automate the movement of the satellites. This would allow for quick reconfiguration between measurements. Automated rotation could be achieved by adding individual stepper motors under each antenna pole. A consideration has to be made if this automation adds a lot of benefit to the testbed. If a lot of measurements are required for the algorithms it is probably desired to automate the movement of the satellites.

8.3 Concept ideas

Three rough concepts were thought out as possible designs for the physical construction. Complete designs of these concepts were not created due to the lack of available time during this thesis project. However, the ideas can be used for the final design of the testbed. The concepts have a different trade-off between complexity of construction and freedom in reconfigurability.

Rotating grid

The first concept for the physical construction consist of a plate capable of rotating with holes in which the Observational antenna systems could be placed. The antenna poles could be rotated inside the holes of the plate as well. Figure 8.1a shows what the concept would look like. The holes would be in a square grid spaced about 12 to 15 cm apart. The spacing may be determined by the amount of positions desired for the Observational antenna systems. As the maximum baseline distance of the testbed is about 1.20 m, a 10 cm spacing would give a 12 by 12 grid with 144 holes, which would probably be more than enough positions. Allowing the plate to rotate would add an extra dimension for positioning relative to the Astronomical source.

Tracks

If automated reconfigurability is desired the Observational antenna systems could be placed onto small tracks instead. The poles could be moved by motors similarly to the movement of the head of a printer or scanner. Figure 8.1b shows a sketch of the concept. The tracks could be placed parallel on a plate that is, just as in the previous, concept capable of rotation. The mock-ups can be swapped between the rails and individually rotated by stepper motors. The biggest advantage of this concept compared to the grid is the quick reconfiguration of the satellite mock-ups as one would not have to walk up to the testbed and replace or rotate each of the antenna poles after every measurement. The main disadvantage of this concept is the increased construction complexity. Also the tracks would increase the difficulty to make the setup stable enough for accurate measurements.

Concentric disks

To get a lot of freedom in movement of the mock-ups the Observational antenna systems could be placed on concentric disks as shown in Figure 8.1c. The disks can be individually rotated to allow for various different configurations. Just like in the previous concepts, the choice could be made to also add stepper motors to the bottom of each antenna pole to individually rotate the antennas.

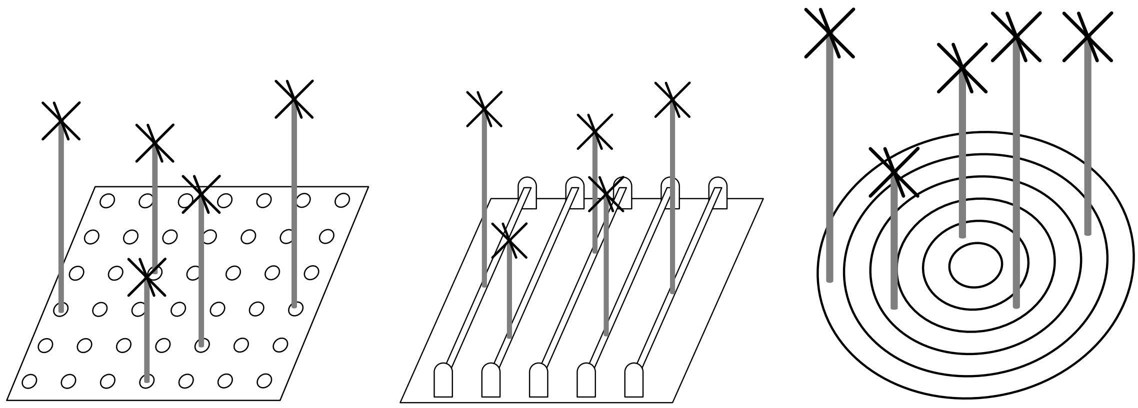

(a) Grid *(b)* Rails *(c)* Concentric Disks

Figure 8.1: Physical construction concepts

8.4 Design review

After the three designs were presented to the supervisor Pieter van Vugt, it was concluded that the first concept was very similar to what Brethouwer had designed during his thesis project. Berthouwers design contained a rotating platform with a circular grid for the Observational antenna systems to be placed in. His design can be seen in Figure 8.2.

Two improvements could be made to Brethouwers design for the physical construction. The first one being that Brethouwer uses a circular rotating platform instead of a square one. A square platform with a square grid might give a little more flexibility for positioning the constellation. Besides that a square grid is easier to construct and define. Secondly, Brethouwer placed the rotating platform on a X-shaped base structure. This base structure could be replaced by triangular base which has the advantage being more easily levelled and stableised using a screw on each corner of the triangle.

The design of Brethouwer for the physical construction is rather complete. The above suggestions might be added to improve it. However the main idea behind the design is clear and only needs to be worked out in detail before it is constructed.

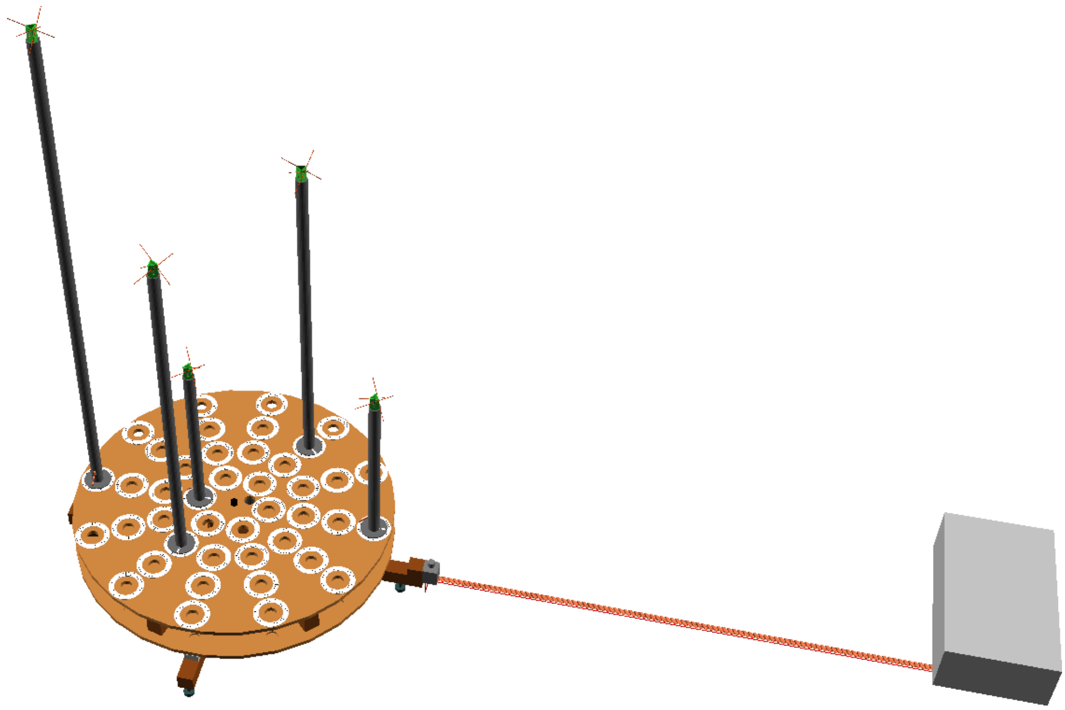

Figure 8.2: Physical construction concept of Brethouwer

8.5 Conclusion

Brethouwer created one concept design for the physical construction of this testbed in his thesis. He suggested that additional concepts should be created for the construction such that the most suitable concept could be selected. During this thesis three additional concepts were created without the knowledge of Brethouwers original design. After reviewing Brethouwers concept with the three additional concepts, one of these concepts was very similar to Brethouwers design. Both contain a rotating plate with a grid of holes in which the Observational antenna systems could be placed and rotated. The two other rough concepts created during this thesis project both have the disadvantage of being more complex to create, with the third one having the most complex construction. The second option uses rails which might decrease stability and accuracy if not a lot of detail is put into the construction. Because of these reasons the first concept, combined with Brethouwers ideas is the best suitable design for the physical construction of the testbed.

The next step for the physical construction would be to create a final design for the physical construction by combining the ideas given in this chapter with Brethouwers design. After that the design is ready to be constructed.

Chapter 9

Conclusions and recommendations

This final chapter is aimed to provide the reader with the insights and conclusions gained during this bachelor's thesis. The research question of this thesis will be discussed for each of the components of the testbed. This research question was: *"What are the unfinished parts of, and open issues with Brethouwer's design for the OLFAR testbed, and how can the design best be completed and implemented?"*, The chapter will conclude with providing a small section of recommendations for future follow-up work.

9.1 Individual results

The aim of this thesis project was to find the unfinished parts of the testbed and see how they could best be completed and implemented. In the following subsections the conclusions for each part of the testbed are discussed with regard to the research goal of this thesis.

At the current state of the testbed, no further research is required for completion of the testbed. One important remaining issue that could not yet be solved is improving the loop filter of the PLL in the receivers. However, provided with the suggestions for improvements that were given in Chapter 6 this problem can be solved.

The remainder of work on the testbed consists mostly of finalizing designs for the physical construction and building the remainder of components of the testbed. The design of the testbed as it is now meets all specifications and should once constructed be able to fulfil all of the tasks required to test the algorithms for calibration and RFI mitigation.

9.1.1 Observational antenna system

Brethouwer designed and simulated an Observational antenna system representing the antennas of a satellite in OLFAR. Of his design a prototype was to be made and characterized. Small modifications were made to Brethouwer's design after which a prototype has been build and fully characterized. From the characterization of the prototype it can be concluded that the prototype met all the specifications initially set up by Brethouwer. The design of the Observational antenna system is therefore suitable to be used in the testbed. The only remaining task is to build four more Observational antenna systems.

9.1.2 Astronomical source simulator

The antenna to be used in the Astronomical source simulator was build by Brethouwer. However, he used an expensive vector signal generator to create the required band-limited noise signal. During this thesis the possibility to use the Nuand bladeRF to generate this signal was explored. It was concluded that the bladeRF is a suitable replacement for the vector signal generator. A remaining task is to measure the quality of the circular polarized signal from the source antenna by measuring the axial ratio. Optionally a second antenna can be added so that arbitrarily polarized signals could be generated as well.

9.1.3 Receivers

The loop filter inside the PLL used for clock synchronisation of the receivers in the proved to be inadequate. A research goal was set to find how this loop filter could be improved. A list of possible improvements were presented, however due to a lack of available time during this thesis these improvements are yet to be implemented. The next step is to implement the suggested loop filter improvements to see if they solve the open issue. Further research into this topic is not required unless the suggested improvements do not fix the current problem with the loop filter. If the issue with the loop filter is solved the testbed can be expanded with 12 more receivers.

9.1.4 Software

The software of the testbed is in a state where the algorithms could be easily implemented. Currently there are no apparent issues regarding the software of the testbed. Therefore, the software was kept unchanged, but a few suggestions were made for improvements. A manual is provided with the thesis which explains how new functionality should be added to the testbed in accordance to the software updates of the receivers since Brethouwer finished his thesis.

9.1.5 Physical construction

Three brief concepts designs were created to provide new views on the physical construction of the testbed. One of these concepts was very similar to Brethouwer's concept design, containing a rotating grid in which the Observational antenna systems can be placed and rotated. Because these concepts were so similar it can be concluded that this concept is the best suitable option for the physical construction. The next step is to finalize the design and building the construction.

9.2 Recommendations

Even though most of the design and research for the testbed is done there are a few essential tasks left to be done during future work. These essential tasks are summarized below:

- Measure the axial ratio of the antenna of the Astronomical source simulator
- Construct four more Observational antenna systems
- Implement the suggested improvements of the loop filter inside the PLL
- Add an additional 12 receivers to the testbed
- Finalize and construct the design for the physical construction

Brethouwer also specified some optional recommendations for future work to increase the functionally of the testbed. One of which was already satisfied during this thesis project, namely implementing a cheaper signal generator for the Astronomical source simulator. The other two optional recommendations are listed below:

- Add a second antenna and signal generator to the astronomical source simulator to generate any arbitrary form of polarization
- Automate the movement of the satellite constellation between subsequent measurements

Bibliography

[1] R. T. Rajan, S. Engelen, M. Bentum, and C. Verhoeven, “Orbiting low frequency array for radio astronomy,” in *Aerospace Conference, 2011 IEEE*. IEEE, 2011, pp. 1–11.

[2] OLFAR & DCIS design team, “OLFAR strawman design report,” ASTRON, Tech. Rep., January 2013.

[3] R. T. Rajan, M. Bentum, A. Gunst, and A. Boonstra, “Distributed correlators for interferometry in space,” in *Aerospace Conference, 2013 IEEE*. IEEE, 2013, pp. 1–9.

[4] M. Brethouwer, “Design of a testbed for the calibration and RFI mitigation algorithms used in OLFAR,” February 2015.

[5] K. Rohlfs and T. Wilson, *Tools of radio astronomy*. Springer Science & Business Media, 2013.

[6] G. B. Taylor, C. L. Carilli, and R. A. Perley, “Synthesis imaging in radio astronomy ii,” in *Synthesis Imaging in Radio Astronomy II*, vol. 180, 1999.

[7] A. R. Thompson, J. M. Moran, and G. W. Swenson Jr, *Interferometry and synthesis in radio astronomy*. John Wiley & Sons, 2008.

[8] M. Garrett. (2016, Januari) Basics of radio interferometry & aperture synthesis. [Online]. Available: https://www.astron.nl/~mag/dokuwiki/lib/exe/fetch.php?media=radio_astronomy_lec_4_ma_garrett.pdf

[9] P. van Vugt, A. Budianu, A. Meijerink, and M. Bentum, “Calibration approach of the OLFAR space based radio telescope,” in *Proceedings of the 65th International Astronautical Congress*, Toronto, Canada, September 2014.

[10] A. Budianu, A. Meijerink, M. J. Bentum, D. M. Smith, and A.-J. Boonstra, “Antenna architecture of a nano-satellite for radio astronomy,” in *Aerospace Conference, 2014 IEEE*. IEEE, 2014, pp. 1–10.

[11] J. Galluppi, "Field probe," Nov. 6 2012, uS Patent 8,305,282. [Online]. Available: https://www.google.com/patents/US8305282

[12] C.I.F. Fr4 data sheet. [Online]. Available: http://www.farnell.com/datasheets/1644697.pdf

[13] Isola. I-tera mf rf datasheet. [Online]. Available: http://www.eurocircuits.com/clientmedia/ecImage/Document/I-Tera-MT-RF-Very-Low-loss-Laminate-Isola.pdf

[14] C. A. Balanis, *Antenna theory: analysis and design*. John Wiley & Sons, 2005, vol. 1.

[15] D. M. Smith, M. J. Arts, A.-J. Boonstra, and S. J. Wijnholds, "Characterisation of astronomical antenna for space based low frequency radio telescope," in *Aerospace Conference, 2013 IEEE*. IEEE, 2013, pp. 1–9.

[16] Nuand. (2016, January) Bladerf product brief. [Online]. Available: http://nuand.com/bladeRF-brief.pdf

[17] Dc offset and iq imbalance correction. [Online]. Available: https://github.com/Nuand/bladeRF/wiki/DC-offset-and-IQ-Imbalance-Correction

[18] S. Haykin, *Introduction to analog and digital communications*, 2nd ed. Hoboken, N.J: J. Wiley & Sons, 2007.

[19] S. Araji, *Digital phase lock loops architectures and applications*. Dordrecht: Springer, 2006.

[20] B. Razavi, "Challenges in the design high-speed clock and data recovery circuits," *IEEE Commun. Mag.*, vol. 40, no. 8, pp. 94–101, aug 2002. [Online]. Available: http://dx.doi.org/10.1109/MCOM.2002.1024421

[21] Nuand. (2013, March) Bladerf schematics. [Online]. Available: https://nuand.com/bladerf.pdf

[22] D. Abramovitch, "Phase-locked loops: A control centric tutorial," in *Proceedings of the 2002 American Control Conference*. IEEE, 2002.

[23] R. E. Best, *Phase Locked Loops: Theory, Design, and Applications*. Mcgraw-Hill (Tx), 1996.

[24] V. Kratyuk, P. K. Hanumolu, U.-K. Moon, and K. Mayaram, "A design procedure for all-digital phase-locked loops based on a charge-pump phase-locked-loop analogy," *IEEE TRANSACTIONS ON CIRCUITS AND SYSTEMS PART 2 EXPRESS BRIEFS*, vol. 54, no. 3, p. 247, 2007.

[25] R. T. Rajan, M. Bentum, and A.-J. Boonstra, “Synchronization for space based ultra low frequency interferometry,” in *Aerospace Conference, 2013 IEEE*. IEEE, 2013, pp. 1–8.

[26] S. V. Engelen *et al.*, “The road to OLFAR - a roadmap to interferometric long-wavelength radio astronomy using miniaturized distributed space systems,” in *Proceeding of the 64th IAC International Astronautical Congress, Beijing, China*. Beijing, China: IAF, August 2013, pp. 1–7.

[27] A. Budianu, A. Meijerink, M. J. Bentum, D. M. Smith, and A.-J. Boonstra, “Antenna architecture of a nano-satellite for radio astronomy,” in *Aerospace Conference, 2014 IEEE*, March 2014, pp. 1–10.

[28] Anaren. Model b0430j50100ahf. [Online]. Available: https://www.anaren.com/sites/default/files/B0430J50100AHF_DataSheet_RevA.pdf

[29] D. Pozar, *Microwave Engineering, 4th Edition*. Wiley, 2011.

Appendix A

OLFAR specifications

Table A.1: The relevant specifications of OLFAR for the testbed [4, App. A]

Property	Specification OLFAR
Spectral specifications	
Frequency range	0.3–30 MHz [2]
Instantaneous bandwidth	10 MHz [2]
Spectral resolution	1 kHz [2]
Timing specifications	
Snapshot integration time	$\geq$ 1 s [2]
Allan deviation (1 s integration time)	$\leq 10^{-8}$ [25]
Deployment specifications	
Deployment location	Earth-Moon Lagrangian 2 point [26]
Deployment configuration	3D Lissajous swarm [2]
Spatial specifications	
Number of satellites	50 (minimum $\geq$ 5) [2]
Baseline length	≤ 100 km [2]
Baseline stability during snapshot	$\lambda/10$ m [2]
Baseline determination accuracy	$\leq \lambda/10$ m [2]
Spatial resolution	Diffraction limited [2]
Aperture filling distribution, snapshot	3D even distribution [2]
Aperture filling distribution, integrated	3D even distribution [2]
Receiver specifications	
Receiver sensitivity	Sky-noise limited [2]
Number of receivers per node	3 [2]
Antenna concept	Active short antennas [27]
Antenna length	9.6 m [27]
Antenna orientation	Arbitrary, but known within $1/60$ rad [2]
Antenna spinning rate	$\leq 1/60$ rad/s [2]
Signal processing specifications	
Imaging procedure	Aperture synthesis [2]
Imaging signal processing	Correlations followed by spatial Fourier transforms [2]
Delay compensation	No [2]
Phase compensation	Yes, off-line for all-sky images [2]
Real-time processing bandwidth	$\geq$ 1 MHz [2]
Required No. ADC bits	$\geq$ 1 bit (dependent on RFI levels) [2]
No. signal bits at correlator	$\geq$ 1 bit (after RFI mitigation) [2]

Appendix B

Construction of the Observational antenna prototype

This appendix documents the construction process of the Observational antenna prototype. It is provided so that in the future multiple Observational antenna systems can be constructed

B.1 Changes made to the original design

Some improvements were made to Brethouwers original design to allow easier construction. Brethouwers design of the Observational Antenna Prototype can be seen in Figure B.1a. This design has been inspired by the patent of a field probe antenna [11]. Each Observational Antenna has three orthogonal dipoles mounted on top of a pope. The dipoles are each mounted on PCBs and are angled $54.7°$ with respect to the vertical feed line. This angle ensures that the influence of the feed lines on all three antennas are equal [4, Ch. 5.2].

The PCBs are mounted as an equilateral triangle on top of a PVC pipe. This pipe has an outer diameter of 32 mm and an inner diameter of 27 mm. The three feed lines, one for each antenna, run from the PCBs through the center of the pole to the bottom. Every 6 cm (quarter wavelength) there is a ferrite core placed on the feed lines to suppress common mode currents. The ferrites are spaced using PVC pipes that are regularly used for electrical installations. These pipes have a 16 mm outer and 14 mm inner diameter. The first 6 cm of the feed lines are completely filled with ferrites to further suppress common mode currents.

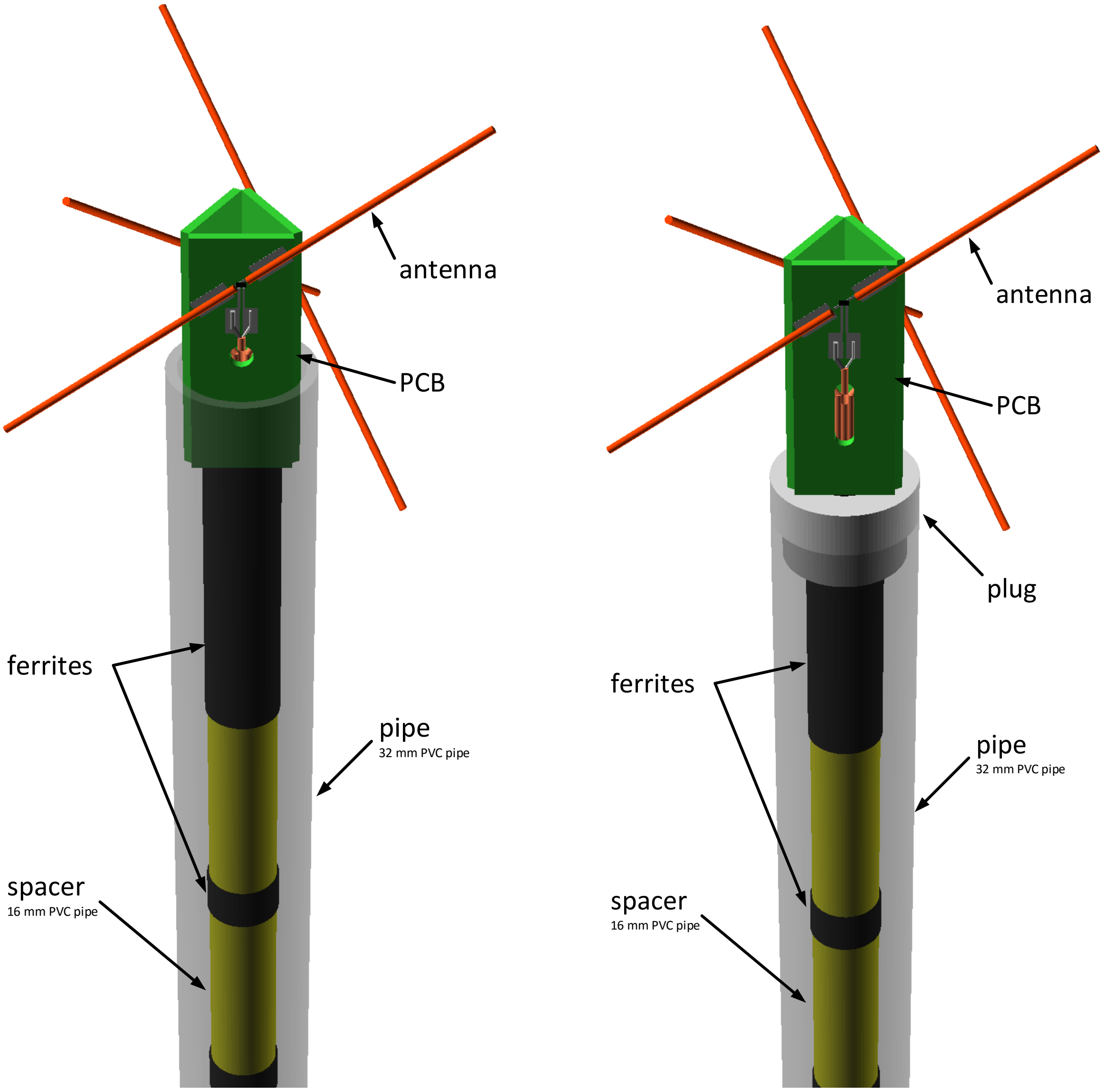

(a) Brethouwers design

(b) Modified design

Figure B.1: Comparison between Brethouwers design and final design

Originally Brethouwer designed the antenna PCBs to be mounted on the inside of the PVC pipe. To allow for easier construction a plug was added on top of the PVC pipe on which the antenna PCBs could be mounted. This plug is shown in white in Figure B.1b. Also a plug at the bottom of the antenna pole has been added to support the stack of ferrites and PVC pieces and allow for the antenna to be mounted on a stepper motor.

Instead of a round hole, a slot was routed in the middle of the antenna PCB, as shown in Figure B.2. This way the feed lines do not have to be forced into tight bends which would cause tension on the solder pads.

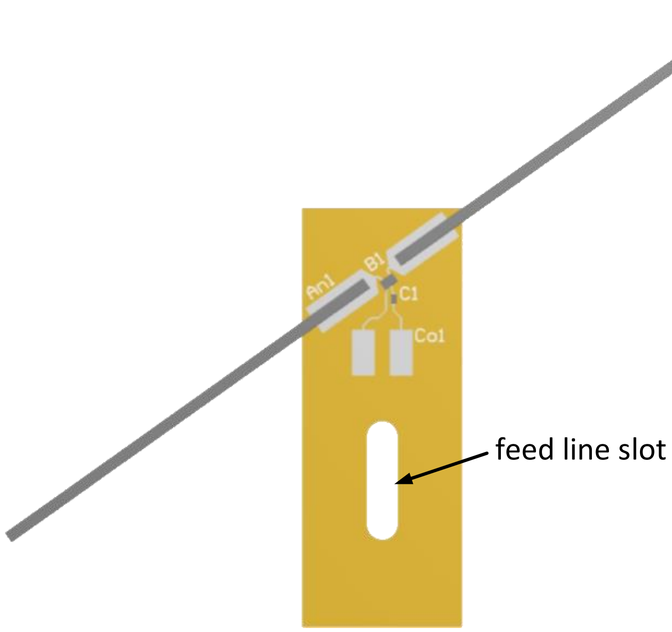

Figure B.2: Final antenna circuit board design

On the antenna PCB there are pads for mounting the dipole, a balun, a capacitor and solder pads for the coaxial cable. The balun was a standard balanced 100 Ω to unbalanced 50 Ω version in a surface mount device (SMD) package. A 10 pF capacitor was added between the feed lines and the balun as was specified by the data sheet of the balun [28].

The type of PCB material was chosen to be standard FR-4. Instead of using copper rods for the antenna dipoles, 3 mm brass rods were used because these were available at the self service workshop.

B.2 Construction

The antenna prototype was constructed in the self service workshop on the University of Twente using materials bought by the local hardware store. First the PVC pipe that had to form the antenna pole was cut to a size of 98 cm. With the two plugs this would give the pole a total length of 1 m.

Both top and bottom plugs have a height of 20 mm, of which 10 mm is placed inside the pipe. Each have a side of 10 mm which has a diameter of 27 mm, allowing them to be mounted inside the PVC pipe. The other side has a diameter of 32 mm which corresponds to the outer diameter of the PVC pipe. Figure B.3 shows transparent 3D models of the constructed plugs.

The plugs were milled on a turning lathe from a 35 mm cylindrical piece of PVC. For the bottom plug first the cylinder was first milled to 32 mm after which the first 10 mm of the cylinder were milled to 27 mm. A 6 mm hole was drilled 20 mm deep through the center of the cylinder to form a hole for the stepper motor. A second hole of 16 mm diameter was drilled only 10 mm deep. This second hole is used to mount the first PVC spacer into. Finally the plug was sawed from the cylindrical piece at 20 mm from the end and a 2.5 mm hole was added to the thicker part of the plug. This hole allows for an imbus adjusting screw to be inserted to secure the stepper motor.

The top plug was made similarly as the bottom plug, only now one hole with a diameter of 17 mm was drilled 20 mm deep. This diameter corresponds to the outer diameter of the ferrites. This way the first ferrite could be mounted flush with the top of the plug touching the bottom of the PCBs.

Fourteen 50 mm PVC spacers were sawed to space the ferrites. Each ferrite has a height of 10 mm, using the 50 mm PVC spacers the center of the ferrites would be separated 60 mm. The stack of ferrites and separators was laced on the feed lines starting with the top plug and seven ferrites. Figure B.4a shows the top of the stack before it was glued into the PVC pipe.

The bottom spacer has a length of 80 mm and has a hole on the side through which the feed lines are guided. A similar hole was drilled in the outer PVC pipe. The bottom spacer was mounted in the bottom plug as shown in Figure B.4b. After all the ferrites and spacers were in place the top and bottom plugs were glued onto the PVC pipe using PVC installation glue.

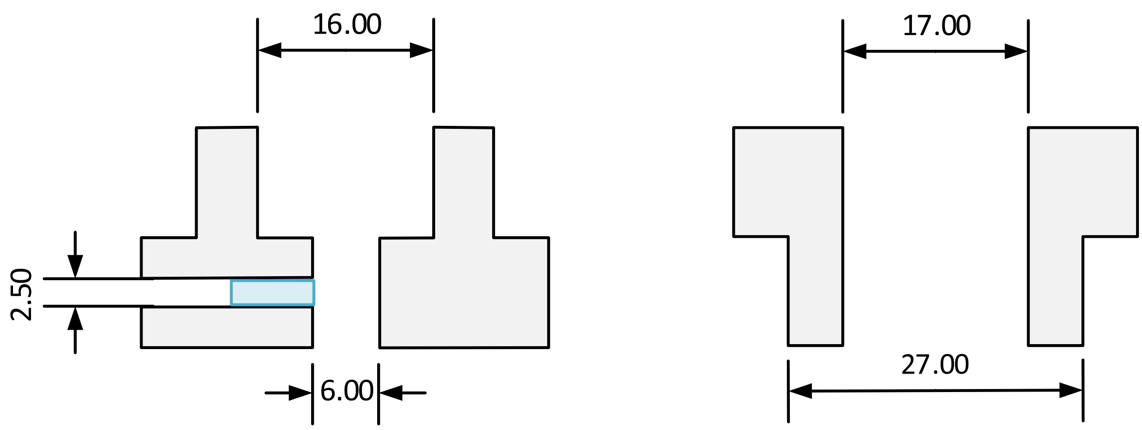

(a) Bottom plug

(b) Top plug

Figure B.3: Schematic 1D drawings of top and bottom plugs.

(a) Ferrite and spacer stack inside the antenna pole

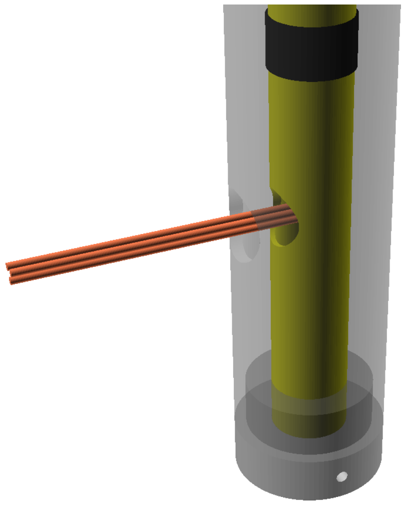

(b) Bottom of stack

Figure B.4: Detailed pictures of ferrite and spacer stack

The antenna PCBs were manufactured by Eurocircuits, without solder-mask or text overlay. These were not necessary in the design and made the costs of the PCBs less. The edges on the back side of the PCB were sanded to an angle of $30°$ so that they could be easier placed in the equilateral triangle. After soldering the baluns, capacitors, dipoles and feed lines, the antenna PCBs were glued in at triangle using hot glue. Finally the triangle of antenna PCBs was hot glued on top of the antenna pole completing the construction of the Observational Antenna prototype. A picture of the finished Observational Antenna prototype is shown in Figure B.5.

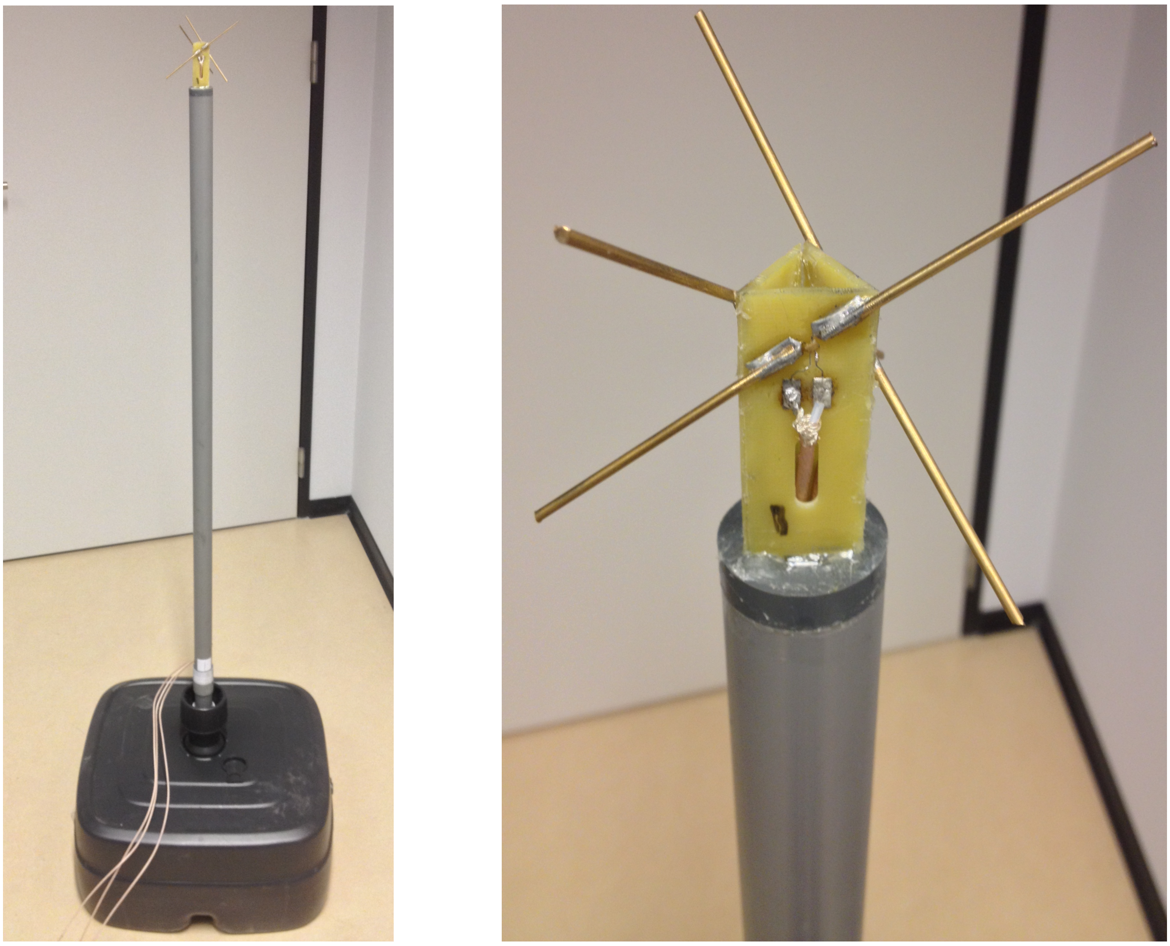

(a) Full overview

(b) Top view

Figure B.5: Finished Observational Antenna prototype

B.3 Recommendations

To align the antenna PCBs in an equilateral triangle the edge on the back side of each PCB had to be sanded in 30° angles and glued together with hot glue. This was tedious and non precise work. To improve this slots could be added to the PCB as shown in Figure B.6a. The PCBs could then easier be aligned as shown in Figure B.6b.

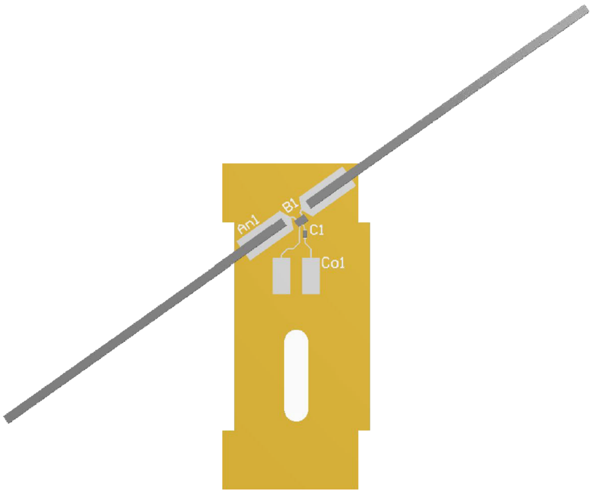

(a) PCB with slots

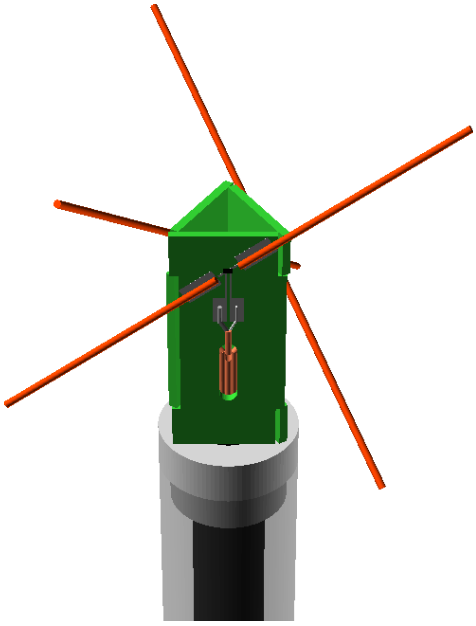

(b) Antenna top with slotted PCBs

Figure B.6: Slotted PCB improvement

For the antenna prototype it was chosen not to use any solder-mask as it was not necessary for the prototype and made the PCBs cheaper to produce. If the testbed will be used outside however, it is recommended that a solder-mask is applied to the PCBs to protect the traces from corroding.

Appendix C

BladeRF x40 specifications

Table C.1: BladeRF x40 specifications [4, Ch. 6]

Name	Nuand BladeRFx40
Price [USD]	420
Spectral specifications	
Frequency range [MHZ]	300 to 3800
Instantaneous bandwidth [MHZ]	28
Timing specifications	
Oscillator type	Factory calibrated 38.4 MHz VCTCXO controlled via 16-bit DAC
Oscillator accuracy [PPM]	1
Signal processing specifications	
Sampling rage [MSPS]	40
Number of ADC bits	12
Spurious free dynamic range [dBc]	60
Technical specifications	
Input connector	SMA (50 Ω)
Onboard processing power	200 MHz ARM9 Processor, Altera Cyclone 4 FPGA
Software support	MATLAB, Simulink, GNU Radio, SDR#
Extras	Transmit capable (full duplex), External clock in-put, External clock output, Expansion header

Appendix D

S-Parameters

An useful description for an N-port network can be given by the scattering parameters, or S-Parameters. These parameters give a full description of the network seen by its N ports [29, Ch. 4.3]. The S-Parameters can be used to describe the efficiency of a transmit and receive antenna pair, which is a 2-port network. The Astronomical source antenna and the Observational antenna system are can therefore be considered as a 2-port network. Figure D.1 shows a diagram of such a 2-port network.

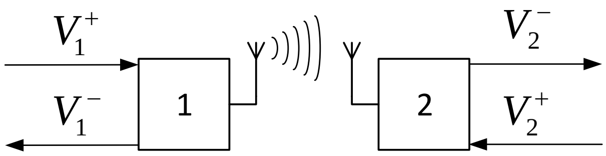

Figure D.1: Two port network consisting of a transmitting and receiving antenna

From wave theory it is known that a wave approaching an impedance change or impedance mismatch can be partially reflected. The S-parameters described the ratios between incident voltage waves (denoted with a V^+) and reflected waves (denoted with a V^-). Their relations are given in the scattering matrix

$$\begin{bmatrix} V_1^- \\ V_2^- \end{bmatrix} = \begin{bmatrix} S_{11} & S_{12} \\ S_{21} & S_{22} \end{bmatrix} \begin{bmatrix} V_1^+ \\ V_2^- \end{bmatrix}. \tag{D.1}$$

An element of the scattering matrix can be evaluated as

$$S_{ij} = \left. \frac{V_i^-}{V_j^+} \right|_{V_k^+=0 \ for \ k \neq j}, \tag{D.2}$$

which means that scattering parameter S_{ij} can be found by driving port j with an incident wave of voltage V_j^+ and measuring the reflected wave amplitude V_i^- out of port i. The incident waves on all ports except the jth port are set to zero, and all other ports are terminated with matched loads to avoid reflections [29, Ch. 4.3].

For a 2-port, the S-Parameters have specific names:

$S_{11} = \frac{V_1^-}{V_1^+}\Big|_{V_2^+=0}$, is the input port voltage reflection coefficient

$S_{12} = \frac{V_1^-}{V_2^+}\Big|_{V_1^+=0}$, is the reverse voltage gain

$S_{21} = \frac{V_2^-}{V_1^+}\Big|_{V_2^+=0}$, is the forward voltage gain

$S_{22} = \frac{V_2^-}{V_2^+}\Big|_{V_1^+=0}$, is the output port voltage reflection coefficient

A VNA is a measurement instrument can directly measure the S-Parameters for 1-port or 2-port networks. It sends out an incident wave with a voltage of $V+$ to one of the ports of the network and measures the wave coming out of all the two ports. The incident waves V^+ and reflected waves V^- can have different magnitudes and phases resulting in complex values for the S-Parameters.The VNA can measures the incident and reflected waves and calculates the magnitude and phases of the S-Parameters.

When an antenna pair is considered as a 2-port the first port would be the input of the transmitting antenna, while the second port is the output of the receiving antenna. Because of mismatch between the output impedance of the transmitter and the input impedance of the transmitting antenna some of the power is reflected back into the transmitter, while the rest is radiated as electro magnetic waves via the antenna. The ratio between the input power and reflected power is defined in the S_{11} parameter. Part of the radiated power by the transmitted antenna is received by the receiving antenna. The ratio between the input power at port 1 and the received power at port 2 is defined in the S_{21} parameter.

Because of reciprocity the S_{22} parameter is similar to the S_{11} parameter and just as important, however now applying to the receiving antenna. The output wave of the receiving antenna is reflected at the input of the receiver. Only some of the power is fed to the receiver while the rest is reflected back into the antenna. When measuring the S_{22} and S_{12} parameters a similar approach is taken as in the first situation, only now an incident is send into port 2, basically doing the measurement the other way around.

The VNA can measure the S parameters of the antennas across frequency, resulting in a plot in which the magnitude and phase of the S-parameter are expressed against the frequency. This plot shows on which frequencies the antenna operates according to the value of the S_{11} or S_{22} parameter. A lower value at a certain frequency would mean that less of the incident wave is reflected and more is radiated by the antenna, resulting in a better performance.

D.1 Voltage Standing Wave Ratio

For a transmitting as much power should be radiated by the antenna, thus keeping reflections to a minimum. Therefore the antenna should be perfectly matched, meaning have the same impedance (or conjugate impedance if the impedance is complex) as the transmitter or receiver. One of the specifications of the efficiency of an antenna is then therefore related to the grade of reflection when connected to a impedance and is directly calculated from the S_{11} parameter [14]. This specification is often given as the VSWR and can be calculated as followed

$$VSWR = \frac{1 + |S_{11}|}{1 - |S_{11}|}, \tag{D.3}$$

where $|S_{11}|$ is the magnitude of the input port voltage reflection coefficient.

The VSWR is directly related to the standing wave that occurs in the transmission lines on a mismatch. If a continuous incident wave is applied to the port the addition of the reflected wave will create a standing wave in the transmission line with minima and maxima. The VSWR then is the ratio between the minima and maxima of this standing wave.

As explained by the previous section, due to reciprocity the VSWR of the receiving antenna is just as important as that of the transmitting antenna. The VSWR of the receiving antenna is calculated by replacing S_{11} with S_{22} in Equation D.3.

D.2 Return loss

Another parameter for an antenna is called the return loss. It expresses the amount of reflected power that is not radiated in the antenna which counts as a loss for the power efficiency. The power of the reflected wave is eventually lost in the resistive losses of the transmission line or the output impedance of the receivers. This loss is called the return loss and can be expressed in dB as followed [14]

$$Return\ Loss = 10\ log_{10} \left| \frac{1}{S_{11}^2} \right| = -20\ log_{10} \left| S_{11} \right|, \tag{D.4}$$

where $|S_{11}|$ is the magnitude of the input port voltage reflection coefficient.

Similar to the case of the VSWR in the previous section, due to reciprocity the return loss of the receiving antenna is just as important as that of the transmitting antenna. The return loss of the receiving antenna is calculated by replacing S_{11} with S_{22} in Equation D.4. Both losses are detrimental to the efficiency of the transmission.